12-13-2019

A modular open-source pre-processing tool for finite element simulations of additive manufacturing processes

William Furr

A modular open-source pre-processing tool for finite element simulations of additive manufacturing processes

By

William Morris Furr

A Thesis
Submitted to the Faculty of
Mississippi State University
in Partial Fulfillment of the Requirements
for the Degree of Master of Science
in Mechanical Engineering
in the Department of Mechanical Engineering

Mississippi State, Mississippi

December 2019

A modular open-source pre-processing tool for finite element simulations of additive manufacturing processes

By

William Morris Furr

Approved:

_____

Matthew W. Priddy
(Major Professor)

_____

Linkan Bian
(Committee Member)

_____

Haley R. Doude
(Committee Member)

_____

Yucheng Liu
(Graduate Coordinator)

_____

Jason M. Keith
Dean
Bagley College of Engineering

Name: William Morris Furr

Date of Degree: December 13, 2019

Institution: Mississippi State University

Major Field: Mechanical Engineering

Major Professor: Matthew W. Priddy

Title of Study: A modular open-source pre-processing tool for finite element simulations of additive manufacturing processes

Pages in Study: 58

Candidate for Degree of Master of Science

Additive manufacturing has shown the ability to produce highly complex geometries that are not easily manufactured through traditional means. However, the implications of building these complex geometries regarding thermal history requires more attention. AM process simulations have proven to be computationally expensive and require large amounts of pre-processing to execute. This thesis will start with a review of additive manufacturing along with current modeling efforts. Then, the development of a pre-processing tool for finite element simulations of these processes is presented. It is shown that the pre-processing tool significantly decreases the total time-to-simulation by removing manual steps. Finally, a study using this tool is conducted to analyze the thermal histories of a cube and a cylinder with two different scan strategies and explore differences in resulting thermal history. It is shown that less temperature fluctuations and a lower final temperature result from an offset scan strategy and a cylindrical geometry.

DEDICATION

This work is dedicated to my family. My parents, Randy and Morri Furr, deserve special acknowledgement for supporting me through my early years in college and always encouraging me to persevere. Thank you to my brother, Eli Furr, for being my best friend and always inspiring me to work harder.

ACKNOWLEDGEMENTS

Research was sponsored by the Army Research Laboratory and was accomplished under Cooperative Agreement Number W911NF-12-R-0011-03. The views and conclusions contained in this document are those of the authors and should not be interpreted as representing the official policies, either expressed or implied, of the Army Research Laboratory or the U.S. Government. The U.S. Government is authorized to reproduce and distribute reprints for Government purposes notwithstanding any copyright notation herein.

I would like to thank Dr. Matthew Priddy, Dr. Linkan Bian, and Dr. Haley Doude for allowing me to work on this project and providing me with this Graduate Research Assistantship. Further thanks are due to Dr. Matthew Priddy for taking a chance on me as his grader for Thermo I so long ago while completing my undergraduate degree and again as your student. You have provided expert guidance and support every time I have needed while serving as my advisor. Thank you to Matt Dantin, David Failla, and Ryan Stokes for being my friends throughout this process and always being willing to help when I needed it.

TABLE OF CONTENTS

DEDICATION ii

ACKNOWLEDGEMENTS iii

LIST OF TABLES vi

LIST OF FIGURES vii

CHAPTER

I. INTRODUCTION 1

1.1 Introduction and Motivation 1
1.2 Research Objectives 2
1.3 Organization 3

II. LITERATURE REVIEW 4

2.1 Introduction to Additive Manufacturing 4
2.2 Microstructure of AM Metals 9
2.3 Porosity in AM 10
2.4 Residual Stresses 14
2.5 Modeling Additive Manufacturing 17

III. DEVELOPING THE PRE-PROCESSING TOOL 24

3.1 Pre-Processing Tool 24
3.2 Tool Path Utilization 27
3.3 Mesh Generation 28
3.4 Activation Determination 29
3.5 Input File Generation 30

IV. CASE STUDY 32

4.1 Case Study 32
4.2 Geometries and Scan Strategies 32
4.3 Thermal Analysis 34
4.4 Thermal Model Validation 37
4.5 Simulation Set-up 40

V. RESULTS 42

5.1 Case Study Results 42
5.2 Pre-Processing Tool Results 47

VI. CONCLUSIONS AND FUTURE WORK 50

REFERENCES 51

LIST OF TABLES

Table 2.1 Process parameters and their effects....8

Table 3.1 Summary of the callable Python functions in the pre-processing tool....26

Table 3.2 Pre-processing tool inputs....27

Table 4.1 Goldak equation parameters....35

Table 4.2 Validation simulation processing parameters....38

Table 4.3 Element counts for different regions in each geometry and the total number of elements....41

Table 5.1 Maximum temperature in each layer for each build case....43

Table 5.2 Maximum thermal gradient (°C/mm) at the end of each layer for each build case....46

Table 5.3 Time measurements for major sections of the pre-processing tool for each geometry....47

LIST OF FIGURES

Figure 2.1 Process, structure [32], [33], properties [9] relationship for AM processes.....8

Figure 2.2 Examples of microscale (phase-field [4]), mesoscale (smooth particle hydrodynamics [71]), and continuum scale (finite element analysis) models. 18

Figure 3.1 Overview of the pre-processing framework. 25

Figure 3.3 A schematic showing the progression from the step file, to the partitioning of the part geometry, then meshing the partitioned geometry, and finally the geometry from the Abaqus input file. 29

Figure 3.4 Schematic of the element activation criteria used. i.) shows the top of a thin-wall build, and ii.) shows a side view of the progressive activation. 30

Figure 4.1 Schematic showing a) the cylinder geometry used and b) the cube geometry used in the case study, as well as dimensions in millimeters.....33

Figure 4.2 Schematic of the two scan strategies on each geometry.....34

Figure 4.3 Temperature dependent material properties for Ti-6Al-4V used in the simulations..37

Figure 4.4 Images comparing raw Abaqus output, interpolated values, and a pyrometer image for similar times during the build. 39

Figure 4.5 Temperature profile down the center of the melt pool for layer one of the validation simulation compared to the experimental mean of the pyrometer data for layer one. 40

Figure 4.6 Final meshes for the cube and cylinder geometries created with Gmsh. 41

Figure 5.1 Temperature profile at the end of layer one for each case. 42

Figure 5.2 Temperature profile at the end of layer four for each case. 43

Figure 5.3 Maximum temperature throughout the build for each case. 44

Figure 5.4 Maximum temperature throughout the build comparing different geometries with the same scan strategies. 45

Figure 5.5 Maximum temperature throughout the build comparing different scan strategies with the same geometry. 46

CHAPTER I

INTRODUCTION

1.1 Introduction and Motivation

Additive manufacturing (AM) involves a process by which material is added layer-by-layer until a finished part is produced. This method of manufacturing allows for quick production times for small production runs, the ability to create highly complex geometries, and reduces material waste. AM processes that produce metal parts typically involves a concentrated heat source, such as a laser, to melt the material as it is applied layer-by-layer. These concentrated heat sources induce large thermal gradients resulting in rapid solidification, heterogeneous microstructures, and large residual stresses. To achieve the maximum utility of AM processes, accurate and computationally effective models are required to predict final part properties and tune processing parameters to achieve desired properties.

Modeling AM using finite element analysis (FEA) is non-trivial, given the high thermal gradients, intricate scan strategies, and mass addition during the process. Small element sizes are required to deal with the gradients and material models typically used for stress-strain relations. These complexities present challenges in simulating usable, complex geometries, and large computation times are needed to simulate simple parts [1], [2].

There has been a large push recently to model AM processes at various length scales and analyzing different aspects of the process. Microstructure evolution is simulated through methods such as Cellular Automata, Kinetic Monte Carlo, phase-field, and various material-

specific empirical models [3]–[6]. Research has been published that models the small-scale, powder particle and fluid flow problems in the melt pool to analyze recoil pressure, as well as Marangoni convection caused by thermocapillary flow [7], [8]. However, due to length scale variations, many of these complex phenomena must be approximated to create part-scale simulations. These larger scale simulations are normally completed through FEA [9]–[13]. Most work on FEA of AM processes has looked at simple geometries and often uses linear-elastic-perfectly-plastic material models [10], [11]. These simple geometries and material models overlook the complex residual stress fields that can arise, and the geometry dependent thermal histories associated with AM.

The scan path taken during a build affects the final part properties by directly affecting the resulting microstructure, and by inducing residual stresses. Microstructure solidification follows the tail-end of the melt pool, forming grains dependent on the local cooling rates and thermal gradients [14]. Residual stresses are induced through preferential conduction through the already solidified part, and through a strain mis-match created by applying molten material to a colder, already solidified layer [15]. Part geometry is the main factor in determining the scan strategy, as this decides how the geometry is traced out to fully solidify the part. Since the part geometry and scan strategy affect part properties, it is important to account for these effects when designing a part to be built through AM and to study these affects thoroughly. However, computational inefficiencies associated with AM simulations prevent many complex and larger geometries from being simulated.

1.2 Research Objectives

This work presents the development and use of an open-source tool to easily simulate material deposition in any FEA software that can activate/deactivate elements. First, the

development of modular functions broken into main sections of the pre-processing procedure is detailed. This section is broken into tool-path conversion and analysis, model meshing, and then element activation determination. Following this, a case study examining the effects of scan strategy on thermal history in a cylindrical and a cube-shaped shaped specimen is detailed to demonstrate the utility of the framework.

1.3 Organization

This thesis begins by providing the motivation for this work and outlines the objectives for addressing the research problem. In Chapter II, a literature review is conducted. First a review of AM and a brief overview of the problem is addressed. The literature review addresses the physical phenomena that present a need for this research including thermal history effects, microstructural effects, FEA modeling efforts, and their dependencies on scan strategy and part geometry. In Chapter III, development of the pre-processing tool and descriptions of its use, shortcomings, and potential for improvement are detailed. This section is broken into different subsections for each major part of the pre-processing tool. Chapter IV explains a case study using the pre-processing tool to simulate the thermal history of a cylinder and a cube of similar size with different scan strategies. Results of the simulations are compared, and the computational efficiency of the tool presented in Chapter V. Finally, Chapter VI presents conclusions and future work.

CHAPTER II

LITERATURE REVIEW

2.1 Introduction to Additive Manufacturing

AM encompasses a number of processes that fabricate near-net-shape, three-dimensional objects in a layer-by-layer fashion, directly from a CAD model [16], [17]. Compared to more traditional near-net-shape manufacturing process, (e.g., casting), AM has multiple advantages relevant to the supply chain: (i) on-demand-production, (ii) short design to production times, (iii) parts can possess complex internal features (e.g., interconnected porous structures), (iv) material waste is significantly reduced, (v) some AM technologies can produce functionally graded components, and (vi) AM offers the ability to produce a large catalog of parts from one machine [18]. With these advantages and mechanical properties comparable to wrought and cast components, AM has the potential to transform modern manufacturing as it progresses from rapid prototyping to rapid manufacturing [16], [17].

AM technologies are used with a variety of different materials including plastics, metals, ceramics, composites, and biomaterials. However, special attention has been paid to the AM production of lightweight and specialty metal alloys such as titanium, nickel, and stainless steel alloys, which is the focus of this work [17]. These materials are most often used in small batch runs, custom parts, and complex geometries for light-weighting, where AM processes have a noticeable cost advantage, such as in aerospace industries, motorsports and luxury vehicle components, as well as the biomedical field [16], [17], [19].

AM technologies first entered the commercial sector in 1987 with stereolithography, a polymer printing technology by 3D Systems [20]. Following this, in 1992, selective laser sintering (SLS) was the first metal AM technology to arise commercially [20]. Six years later, in 1998, Sandia National Laboratory began offering their laser engineered net shaping (LENS) system for sale to industry [20]. Since then, directed energy deposition (DED) (e.g., LENS) and powder bed fusion (PBF) (e.g., SLS) processes have dominated research and industry interests in AM production of metal components. PBF uses a laser, typically Nd:YAG or CO_2, to selectively melt each layer from a bed of powder. This powder bed is packed and spread over the substrate, which is lowered for more powder to be spread following each full layer trace by the laser [21], [22]. DED uses simultaneous material deposition and melting from one or more nozzles and a coaxially mounted laser or electron beam [23]. Only the material necessary for the current layer is deposited in DED, although there is some material spatter. Of these two processes, PBF offers better final part density from the powder bed packing, faster laser scan speeds, higher resolutions, and reduces the need for added supports due to the compacted powder bed surrounding the part [24]. The direct deposition capability of DED reduces waste powder to be sifted after production, which must be done in powder bed processes, where the reuse of this sifted powder is limited to some extent. With multiple nozzles or the potential for multiple powder feeders, DED allows the use of multiple materials during a single build to produce functionally graded components with a gradient from one material to another [23], [25].

While AM offers advantages over traditional processing methods, it still has obstacles to overcome before mainstream industry adoption. Laser based AM processes produce a complex, heterogeneous thermal history that drives microstructural morphology, defect production, and resulting residual stresses [23], [25]. This thermal history is characterized by a small, localized

heat source tracing out the part resulting in large thermal gradients, rapid cooling, heterogeneous heat transfer favoring conduction through solidified material, and reheating of material by subsequent layer deposition [26]. A broad array of process parameters, as well as material thermal properties, ultimately determine the thermal history. Some common process parameters include: scan speed, laser power, hatch spacing, scan strategy, and powder feed rate (DED) or powder bed packing (PBF).

Microstructural morphology in AM parts is a heterogeneous mix of elongated grains following the direction of solidification, very fine regions due to high cooling rates, and areas of equiaxed grains near the substrate which acts as a heat sink. However, a heterogeneous microstructure may be an advantage in some applications that require varying material properties throughout a part. Residual stresses arise from the large thermal gradients and subsequent layer depositions, where a strain mis-match can arise from applying molten material to cooling layers. One of the more pressing concerns with AM produced parts is the presence of defects. Defects such as voids, inclusions, and surface roughness are commonly a result of trapped gases, un-melted powder, inadequate adhesion between layers, and a build resolution limited to the layer width. While quite often the defects, residual stresses, and microstructure homogenization are resolvable through post manufacturing processes, costs associated with using AM parts are reduced when minimizing required post-manufacturing processes. To optimize as-built parts in AM, further research and technological development in the field is necessary.

The most cost effective and time-efficient method for researching a physical problem is often through computational modeling and simulation. Modeling allows for the physics of a build to be represented through mathematical equations where results can be analyzed in depth without the need for physical experiments like tension tests or compression tests. Developing a

model takes longer than setting up and running a single physical experiment in most cases, but once the model is developed, hundreds or thousands of simulations could theoretically be run in the time to run one physical experiment. A researcher could use the model to perform parametric studies or variation of inputs very quickly relative to physical experiments. However, AM presents some challenges to modeling the process and to running simulations in an acceptable amount of time with a high enough fidelity to be useful. To accurately model AM processes and the representative physics, one must account for complex boundary conditions, temperature dependent material properties, a spatially distributed heat source, material addition, distortion from thermal stresses, and solid-liquid interactions in and around the melt-pool.

The mechanical strength of materials in the as-deposited condition is a direct result of the final microstructure in the part [27]. Resulting microstructures are not only a result of solidification, but the cyclic heating of subsequent layer depositions can further coarsen grains in some regions [27]. In laser based AM, large cooling and solidification on the order of 5,000-10000 K/s can result as well [23], [27], [28]. This thermal history is controlled by adjustable build parameters and governs the resulting part properties [23], [29], [30]. These parameters control the melt pool characteristics, the heat affected zone, microstructure, porosity, and residual stresses, as laid out in Figure 2.1 [26]. Some of the more important process parameters and brief descriptions of their effects on the part are presented in Table 1. Complex inter-dependencies and large numbers of controlling parameters for part quality present an increased need to model AM processes and simulate potential combinations of parameters [31].

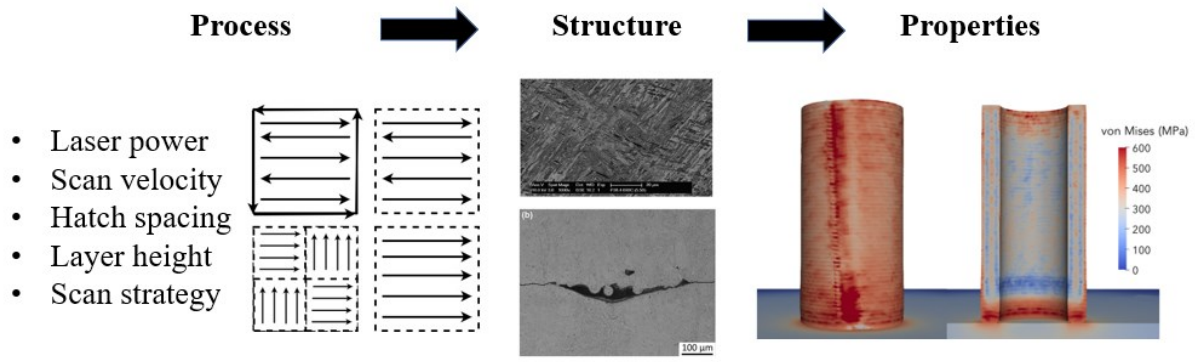

Figure 2.1 Process, structure [32], [33], properties [9] relationship for AM processes

Table 2.1 Process parameters and their effects

Build Parameter	Effects of Adjustments	Sources
Laser Power	• Inversely proportional to cooling rate • Proportional to grain size • Decreasing results in thinning and elongation of the melt pool	[23], [25], [28], [30]
Scan Speed	• Increasing causes thinning and elongation of the melt pool • Proportional to cooling rate. • Proportional to grain size • Inversely proportional to grain width.	[23], [25], [28], [29]
Hatch Spacing	• Reduced bonding between layers when increased	[34]
Scan strategy	• Changes the amount of powder injected in the melt pool for DLD due to offset between laser and powder stream • Affects thermal history, residual stress production, and mechanical properties	[25], [25], [35]–[39]
Shielding Gas Flow Rate (DLD)	• When increased, an initial increase in powder density and layer thickness with transition to decreases	[23]
Powder Feed Rate (DLD)	• Proportional to layer height • Inversely proportional to melt pool depth • Increasing promotes the development of columnar grains	[23], [25], [25], [40]–[42]
Powder Bed Density (PBF)	• Reduces gas entrapment when reduced	[24]

2.2 Microstructure of AM Metals

Any parameter that affects the thermal history of the material will affect the evolution of the resulting microstructure. Process parameters at the beginning of solidification control grain morphology, size, and texture [29]. The resulting grain size is also controlled by cooling rates after solidification, which is further exhibited by a coarsening of microstructure due to post-manufacturing processes involving heating, such as hot isostatic pressing [29], [43]. Solidification follows the direction of heat flow, resulting in varying grain growth directions and crystallographic orientations for AM parts [27]. More specifically, the ratio of the cooling rate to thermal gradient, R, and the temperature gradient at the solid-to-liquid interface, G, have been shown to control the resulting microstructural features of a build [25].

The microstructure plays a significant role in the resulting mechanical properties of produced parts, including strength, ductility, and fatigue life [44]. From the Hall-Petch effect, it follows that finer grains that result from rapid-solidification processes will maintain a higher yield strength [45]. Finer microstructures, which are present in laser based AM components, exhibit better resistance to crack initiation, but promote a flattened crack growth path, which results in inferior high cycle fatigue behavior [23], [46]. However, the resistance to crack nucleation does give AM produced parts better low cycle fatigue behavior [23]. Post manufacturing processes affect the microstructure of the material and mechanical properties [23]. Heat treatments can change the characteristics of the alpha phase in Ti-6Al-4V, which is known to produce softer grain boundaries allowing accelerated crack growth [23], [47].

Microstructures in AM parts follow a general pattern with finer equiaxed or near-equiaxed grains near the substrate, and larger, columnar grains further away with a transitional region between [29], [48], [49]. The fine-grained region near the substrate is attributable to

thermal gradients being more non-linear into the substrate, with these effects being diminished from substrate pre-heating. As the process continues, heat builds and becomes more uniform perpendicular to the build direction, causing solidification to primarily occur in the build direction. Columnar grains primarily dominate these later layers [48]. Further intricacies in microstructures occur when there are multiple stable solid-state phases, such as with Ti-6Al-4V. In Ti-6Al-4V, the large columnar grains are formed as a body-centered-cubic, β-phase [23], [48]. After solidification into this prior beta grain, the material undergoes a solid-state phase transformation around 980°C to a hexagonal closed packed, α-phase [50]. In AM this often forms a fine, basket-weave morphology of mixed alpha and beta phases in the prior beta grains. Sizes of the alpha and beta laths have been shown to vary with location due to varying thermal histories at different sections of a part [23]. Top regions consist mostly of fine lamellae and the bottom, closer to the build plate, has comparatively, thicker lamellae, due to reheating of the middle regions from subsequent laser passes [23]. [48], [50]. This resulting microstructure is attributed to the rapid and directional solidification associated with AM.

2.3 Porosity in AM

Porosity is the presence of voids in a material. There are instances of desired porosity such as in the bio-medical field with additively manufactured Ti-6Al-4V bone implants or if a form of mass transport by a series of interconnected voids through the material is desired [51], [52]. However, these voids are generally viewed as a defect in structural parts produced through additive manufacturing (AM). The presence of voids reduces the density of a part, increases anisotropic behavior in mechanical properties when the voids are non-spherical or unevenly distributed, and causes stress concentrations at the walls of a pore where crack nucleation is likely to occur. Because of porosity induced anisotropy, significantly higher yield strengths are

experienced in loading directions perpendicular to build directions of AM produced parts [43]. The stress concentrations negatively impact the total fatigue life in the high cycle regime by promotion of crack initiation [47]. The observed decrease in fatigue life compared to wrought material relates to an increase in pore size, but more significantly with a decrease in its distance relative to the surface [47]. Improvements to the mechanical properties and anisotropy of AM produced materials has been shown through post-manufacturing processes such as hot isostatic pressing (HIP) [43]. Regarding AM, porosity is often described as either interlayer or intralayer. Interlayer porosity occurs between deposition layers, and intralayer pores are located within the bulk of the deposition layer. Interlayer and intralayer porosity have distinct characteristics and result from different parameters and periods in the manufacturing process.

Intralayer porosity is characterized by spherical pores that are not localized to any given point in the material microstructure [53]. These pores generally result from trapped gas and have multiple likely causes: (i) coalescence of gaseous pores in powder particles formed during powder production, (ii) vacancies resulting from packing limitations of spherical particles in PBF processes, (iii) powder feed gas entrapment from melt pool turbulence and entrainment in DED processes, and (iv) from vaporization of the material in the melt pool. With the high vaporization temperatures of titanium alloys and little turbulence, the most significant causes of intralayer porosity are packing limitations and powder particle porosity. There is a maximum, random close-packed density for spheres of identical size that can be achieved of approximately 64%; therefore, gaps between powder particles is unavoidable [54]. With laser-based AM typically requiring an inert gas atmosphere, often argon, and an inert gas to feed powder, voids between particles will be filled with these local gases which may not have time to escape the molten material during the rapid solidification in laser-based AM.

Packing of powder particles can be a major parameter affecting resulting intralayer porosity. A maximized packing density helps to minimize intralayer porosity by reducing voids between particles that can potentially be filled with gases [55]. Powdered metals are typically sold in size distributions with a range of particle size distributions such as 45-75, 75-105, and 105-150 microns. These distributions often occur from inconsistencies in the production processes, but this can also be intentional. An appropriate distribution of particle sizes with large particles and an adequate number of smaller particles to fill in the vacancies left between larger particles can maximize packing density and lower resulting porosity [55]. However, too large of an amount of smaller particles relative to larger, and the agglomeration of particles, as well as, the resulting positive effects on packing is reduced [24]. Powder layer density can be improved over the manufacturer measured powder density with a proper size distribution and ratio of large to small particles [24]. Spierings and Levy found that a ratio of ten particles per layer thickness led to a powder layer density of about 60%, which is slightly higher than the manufacturer provided density, which was around 58% between different powder variations used in the experiments [24].

More spherical particles are preferred for inherently better packing properties, resulting from lower interparticle friction coupled with higher particle mobility [24]. Powder production methods can play an important role in intralayer porosity. During the gas atomization process, which is the most common method of producing metal powders for additive manufacturing, molten metal is impacted with streams of gas to form droplets (the powder particles). This process can cause gaseous voids to form in the powder particles as well as more irregularly shaped particles. When incident to the melt pool, these local pores will coalesce to form larger gaseous voids inside of the material. Correlations between initial powder porosity and resultant

part porosity have been found in AM produced stainless steel [56]. Utilizing powders produced through the plasma rotating electrode process (PREP) can likely reduce the porosity resulting from packing density limitations and powder particle porosity. Powders produced through PREP have a smoother, more spherical surface, less particle porosity, and have resulted in three times less part porosity and a higher powder feed rate in a study by Ahsan et al [57]. Interlayer porosity is not as well understood as interlayer, but it is generally not as detrimental to the mechanical properties of a material. Intralayer pores caused by trapped gases do not affect the part's ductility, unlike interlayer pores [32], [58].

Interlayer porosity is characterized by elongated, irregularly shaped pores occurring along the boundaries of deposition layers in the laser scan path and possessing an irregular surface [53]. These pores are often attributed to the temperature distribution in the deposition layer following the laser path, resulting in lack of fusion (LOF) between deposition layers [53]. LOF porosity is likely the most detrimental to the mechanical properties and their anisotropy experienced in laser based AM [59].

Since interlayer LOF porosity is in the direction of laser scan path, they are elongated perpendicular to the build direction [59]. This would partially explain the reduced ductility experienced when loaded in tension along the build direction but display of similar elongation to failure, compared to wrought materials, when loaded perpendicular to the build direction [32], [59]. Higher yield strengths are also experienced perpendicular to the build direction. This anisotropy in mechanical properties is effectively reduced through HIP, a process mainly used to reduce porosity and found to reduce LOF porosity in AM produced parts [43], [60], [32]. In critical applications loaded in tension and in the build direction, LOF porosity will be a detrimental factor due to a reduction in the loading area. However, when subjected to a

compressive load, the effects on mechanical properties are reduced as the load is effectively acting towards closing the pores [59].

Due to high cooling rates causing rapid solidification, the heat transfer driving solidification must be carefully controlled to reduce LOF porosity. Achieving the ideal laser parameter settings is the most important factor in reducing interlayer porosity in the as-manufactured state for AM materials [26]. To maintain adequate bonding between layers, proper melting of current deposition layers, as well as re-melting of previous layers must be optimized. Laser parameters are the driving force behind proper layer melting, including laser power, scan speed, hatch spacing, and laser scan path. Hatch spacing, which is the distance between individual laser passes for two parallel deposition layers, has been found to have a noticeable impact on intralayer porosity [34]. Intralayer overlap is reduced with a hatch spacing that is too large, effectively preventing adequate bonding between layers. This lack of bonding results in un-melted powder between layers and interlayer porosity [34]. However, a study did find that this negative effect can be reduced with smaller layer thicknesses [34]. Furthermore, the melting efficiency of the deposited powder is shown to increase with higher laser powers and lower traverse speeds, reducing LOF [25]. Interlayer porosity is largely reconcilable through careful adjustment of process parameters such as laser power and scan speed, as well as post-manufacturing processes such as HIP [23], [43].

2.4 Residual Stresses

Residual stresses are stresses that exist in a material when it has reached an equilibrium with its environment. Residual stresses can occur from uneven deformation of components and materials, in the case of laser based AM, due to large thermal gradients [61]. Residual stresses are generally classified into three types based on the scales at which they occur. Type I residual stresses are

variable of the dimensions of the part and can result in large deformations. Type II residual stresses occur from different phases being present in the material, while Type III are due to dislocations at the atomic scale. Type I have been studied more in depth as they are of larger importance to the strength of a material [62]. Residual stresses, as with porosity are sometimes desired. Glass is produced by purposely introducing compressive stresses in the surface of the plate [63]. Shot peening, pelting a material with metallic balls, to purposefully introduce a compressive residual stress field through plastically deforming the surface has shown to effectively improve fatigue strength in materials [64]. However, for AM produced structural parts, tensile residual stresses generated are generally not desirable and can negatively impact the maximum load a part can reliably withstand, favor crack propagation, decrease fatigue life, and cause warping [23], [62].

Every production process introduces residual stresses to a material, but the stresses introduced can vary greatly among these processes. Laser based processes are recognized to introduce large residual stress fields due to the large thermal gradients created in the heat affected zone, where the laser is incident [26], [62]. It has been shown that AM processes can lead to residual stresses as high as the material's yield strength and sometimes greater [65]. Residual stresses of up to 75% of the yield strength have been found using hole drilling and laser holography, which only measure to a depth less than a millimeter [61], [66]. Two of the mechanisms responsible for residual stresses in AM produced parts are the thermal gradient mechanism and the cool-down phase of the molten top layer [62]. Rapid heating of the upper surface of the material and conduction through the part and substrate facilitates the large thermal gradients [62]. Expansion of the heated upper layer is prevented by the lower, colder previously deposited layer inducing compressive residual stresses. During the cool-down phase, the

previously heated material undergoes thermal contraction which is also prevented by the previously deposited layer, inducing residual stresses [62]. The final stress profile results in tensile stresses at the part surface with compressive stresses at the core [61].

The stress state that occurs could be from the outside of the part being hotter than the interior with the shrinkage of the exterior during cooling being prevented by the interior of the part. With a roughly circular melt pool the heat transfer is circular locally, but part geometry affects this, especially at the edge of the part [26], [61]. At edges, the heat flow is localized and can more readily dissipate through the lower deposition layers, resulting in the edges of the part being hotter during the solidification process, which can develop the axially distribution of residual stresses [61].

The base plate on which the part is built also plays a significant role in residual stresses introduced. The residual stresses are significantly higher before the part is removed from the base plate with stress relaxation occurring upon removal by uniform shrinkage and bending deformation. After removal from the base plate, the stress profile involves tensile stresses at the upper and lower portions of the part near the surface with compressive stresses towards the center [62]. This stress profile, and the fact that the more layers added to the part, the higher the resulting residual stresses will be, may indicate that the residual stresses are aligned with the direction of laser scanning [61], [62]. The largest residual stresses are located at the top of the part, the end of the laser scan path, with the lowest stresses being towards the base plate, at the beginning of the scan path[23], [62]. The temperature on which the layer is being deposited plays a role in resulting residual stresses, since this affects the thermal gradient.

Residual stresses can be effectively reduced through heat treatments, proper selection of process parameters, and heating of the build substrate. It has been shown that by increasing the

incident energy through increasing the laser power and scanning speed, residual stresses can be reduced [65]. Since these two parameters affect other details of the build, such as the size of the heat affected zone and the temperature of the build substrate as well as previously deposited layers, carefully accounting for these factors could be an effective way of reducing residual stresses in AM parts [65]. Various laser scanning strategies with different materials have also been studied and their effects on residual stresses evaluated. It has been found that adjusting the dwell time between laser passes, controlling time for cooling of the deposition layer, can effectively reduce residual stresses in a part [67]–[69]. It has been reported that changing laser scan speeds and power can reduce residual stresses by up to 20% from the yield strength [70]. More noticeable reductions in residual stresses has been noted for preheating of the build substrate, with up to 40% reduction from the yield strength for a preheat to 400℃ [70]. It is likely that larger reductions in residual stresses come from greater base plate temperatures to a degree, as Mercelis and Kruth reported that minimal residual stress reductions did occur from preheating to a temperature of 200℃ [62]. It was also shown that preheating of the base plate reduced the effectiveness of residual stress reduction through changes in laser power and scan speeds and vice-versa [70].

2.5 Modeling Additive Manufacturing

Potential advantages of modeling and simulation have inspired research in modeling the various physical processes in AM at varying length scales. AM has important physical processes to be accounted for at the micro-, meso-, and continuum-scales with some modeling overlapping length-scales. Examples of models looking at each of these scales is shown in Figure 2.2 For the highest fidelity model possible, each of these scales must be accounted for. However, researchers must often make assumptions in their models to make calculations in a reasonable amount of

time. At the micro-scale, microstructural models are used to analyze how the solidified material forms grains and the final material phases. Meso-scale simulations usually analyze powder and melt-pool interactions including Marangoni convection. The continuum scale is the result of the micro- and meso-scale phenomena, which is where residual stress fields, distortion, and overall part properties are accounted for.

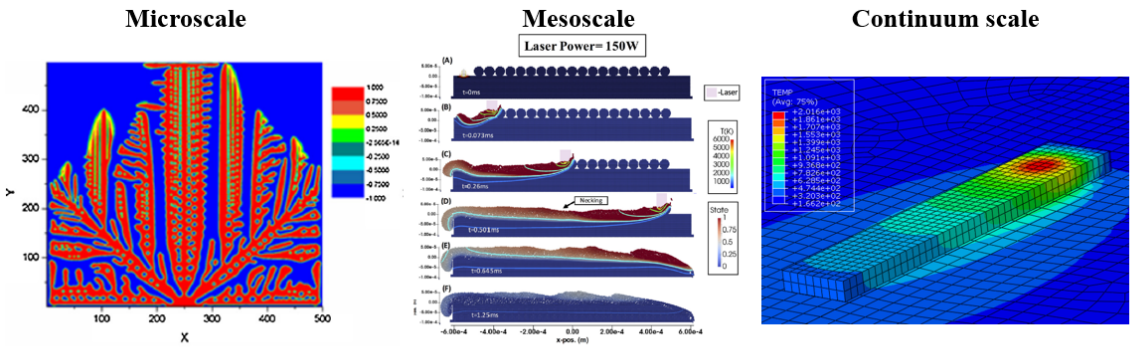

Figure 2.2 Examples of microscale (phase-field [4]), mesoscale (smooth particle hydrodynamics [71]), and continuum scale (finite element analysis) models.

Micro-scale phenomena revolve around material solidification and grain formation. Modeling this has been primarily carried out through phase-field simulations in AM [72]–[75]. Phase field models describe compositional and structural features of the microstructure of a material through a set of field variables that are continuous across diffuse interfacial regions [76]. Phase field modeling can be used to model material solidification, grain growth, and solid-state phase transformations [76]. Phase-field is a high-fidelity modeling technique based in fundamental thermodynamics and kinetics, but it can be computationally expensive [76]. Cellular automata (CA), which incorporates probabilistic components when applied to microstructure prediction, has also been explored for AM [77]–[81]. CA when applied to

microstructure solidification normally uses a probabilistic model for grain nucleation proposed by Rappaz and Gandin [82]. Using this, the domain is divided into cells with each cell having a value representing the phase at that region. With process temperature data, usually from finite-element simulations, and a few rules for how cells interact, the grain solidification is simulating by discretizing over time [82], [83]. CA is more computationally efficient and can calculate 3D microstructures for large parts, but does not account for solid-state grain evolution through the many heat source passes in AM. Rodgers et al. have tried a more novel approach, adapting the Potts Monte-Carlo method to work for electron beam and laser processing [84]. The Monte Carlo Potts model assigns an integer value to each lattice site in the simulation, and neighboring sites with like integer values constitute a grain. Neighboring sites with unlike values contribute to the total energy of the system. System energy is minimized through grain growth where a site is randomly assigned a different integer value, and an acceptance probability is calculated [84]. This method can predict microstructures for large builds and account for multiple heat source passes.

The meso-scale is characterized by the interaction of particles with themselves and the melt-pool, as well as the physics within the melt-pool, such as Marangoni convection. The discrete element method (DEM) has elucidated understanding of particle motion and interaction. Haeri et al. used DEM to study particle packing in a powder bed for a PBF process, characterizing the bed surface roughness and how particle size and spreader velocities affect it [85]. Steuben et al. extended DEM to include heat transfer in the simulation, allowing analysis of the effects of individual particles on the heat transfer in and around the melt pool [86]. Smooth Particle Hydrodynamics (SPH), a mesh-free, Lagrangian numerical scheme has also been adapted to simulate additive processes. Using SPH, Russel et al. explored the effects of thermal conduction

around the scan track, and varying the laser power [71]. Khairallah et al. was able to study the melting of a randomly-distributed bed of powder particles with temperature-induced surface tension in the multi-physics code, ALE3D [87]. In an extended work, the same code was used to analyze spatter, denudation zones, and the formation of pores [7].

The continuum scale will be the focus of the remainder of this work. On the continuum scale, researchers are largely concerned with thermal history of entire parts and resulting residual stress fields. At this scale, lower length scale phenomena coalesce to present complicated boundary and loading conditions to be accounted for in a model. An accurate model will need to account for heat transfer in the form of radiation from the laser, convection into the local atmosphere, and conduction through the part and powder bed for PBF processes. Heat flux from the laser is a main point of concern. The localized heat source creates large thermal gradients that can give convergence issues. From this complicated thermal history, the stress field in the evolving part will be constantly changing from cooling, reheating, and new deposition. The heterogeneous thermal history of the part created by the localized heat source presents further challenges with model calibration and validation. Using thermocouple data from experimental builds will not provide any information about the melt pool, which is the direct cause of final part properties and microstructural morphology [23], [26]. Of continuum scale simulation techniques, the most commonly seen in the literature is finite element analysis (FEA). FEA allows the domain being simulated to be discretized into elements that allow the governing equations to be solved numerically.

Modeling of the laser heat source is one of the most critical elements of building an accurate FEA model of an AM process since this is what governs the thermal history. Most AM modeling efforts presented in the literature use a variation of Goldak's double ellipsoidal heat

source [10]–[12]. This heat source model was originally developed by Goldak et al. to model arc welding, but offers enough adjustable parameters to cover laser and electron beam welding as well [88]. The general form of this is presented below in Eq 2.1 where Q is the applied flux, σ is a gaussian distribution calibration parameter, P is the laser power, η is the efficiency, r is the beam radius, and d is penetration depth. Other models present in literature include a Gaussian volumetric distribution [9] and a conical-shaped Gaussian distribution [89].

$$Q(x,y,z,t) = \frac{2\sigma\sqrt{\sigma}P\eta}{r^2 d\pi\sqrt{\pi}} \exp\left[-\sigma\left(\frac{x^2}{r^2}+\frac{y^2}{r^2}+\frac{z^2}{d^2}\right)\right] \tag{2.1}$$

With temperatures ranging from above liquidus to room temperature, temperature dependent material properties are necessary. For the thermal analysis, all papers reviewed used temperature dependent thermal conductivity and specific heat capacity [9]–[12], [89], while some also used temperature dependent density [89], but this included little variation. Where necessary, mechanical material models used also used temperature dependent data, including: elastic modulus, yield strength, thermal expansion coefficient, and some use temperature dependent Poisson's ratio [10]–[12], [89].

AM processes involve non-negligible amounts of heat transfer through conduction, convection, and radiation. When modeling DED, the literature shows that a combination of forced and free convection should be used for an accurate model. Yang et al. and Lu et al. use constant but different values for the convection coefficients for free and forced convection [12], [90]. Heigel et al. took this a step further and conducted convection experiments on a thin-wall geometry to fit a spatially dependent forced convection model which was shown to give improved results [10]. However, this method requires a different experiment and fitting procedure for different geometries or gas flow rates. Conduction is carried out with temperature

dependent thermal conductivity values as discussed previously. All papers that have been reviewed here use a set value for emissivity to calculate radiation, along with the Stefan-Boltzmann law, with a value of ϵ=0.54 being the most common value used for Ti-6Al-4V [10]–[12]. Since PBF processes do not use a deposition head with shielding gas, a constant value for free convection is enough. However, these processes use reduced thermal conductivity for the powder regions surrounding the part.

Simulation of the addition of solidified material is another difficult matter to approach. There have been three main methods used for DED: activating elements as an entire layer [90], quiet activation [12], and a hybrid quiet/inactive activation method being the most prevalent [9]–[11]. When using the quiet element method, all elements are present throughout the analysis, but when they do not represent solidified material their properties are scaled down to be effectively zero [91]. The inactive method simply removes elements from the analysis until they represent solidified material effectively reducing the degrees of freedom initially, but this method can result in increased computational times from equation renumbering and initialization [91]. Both of these methods can result in artificial heat generation if the nodal temperatures are not reset to ambient at each time step [91]. The hybrid method originally proposed by Michaleris has elements as inactive until the simulations arrives to their layer in which case the elements become quiet until they are to represent solidified material [91].

Model validation and calibration with reliable, representative experimental data is critical to the development of an accurate model. AM is characterized by a complex space and time dependent thermal history. The most representative experimental data to calibrate thermal models would be spatial and time dependent. Literature shows that most researchers are using 2-4 thermocouples to validate their models [10], [12], [90]. Arguably better results could be

obtained from thermal imaging with Wang et al. using CCD camera data and Johnson et al. using IR thermal images throughout the part [9], [89]. Those authors using thermocouples do further validate their thermal models by showing agreement between thermal and mechanical models through further deflection data used to validate mechanical models [10]–[12], [90].

Since the production of complex geometries is one of the main attractions of AM, and geometry dependence of the process thermal history of the process has been shown, it is important to use modeling and simulation to analyze varying and complex geometries. In spite of this need, literature has looked mostly at simple thin-wall geometries [10], [89] or an enclosed-box thin-wall variation [12], [90]. Lu et al. did simulate an S-shaped part, but the simulated parted approximated the curved experimental counterpart with 90 degree turns [90]. The most complex geometry present in literature is the cylindrical tube presented by Johnson et al. [9]. The lack of complex geometries simulated in literature is likely due to difficulties in representing tool paths of complex geometries and computational inefficiencies of simulating the process. Most commercial FEA codes do not offer a direct implementation of the tool path to simulate the moving heat source and element activation. Large thermal gradients in the process create a need for very small elements which results in many elements for an entire part. Current finite element models of AM are computationally intensive, with Fu and Guo reporting a computational time of 240 hours on a standard desktop to model 5 layers with approximately 48,000 elements per powder layer of a thin-wall geometry [92]. Furthermore, complex parts may have an increased amount of surface area which result in surface and corner hot-spots due to preferential conduction through solidified material rather than convection into local atmosphere.

CHAPTER III

DEVELOPING THE PRE-PROCESSING TOOL

3.1 Pre-Processing Tool

The goal of this work is to provide a pre-processing tool for preparing finite element simulations of AM processes while maintaining modularity and using open-source software. This tool was developed to meet four main needs in pre-processing AM simulations. Firstly, the tool uses a common machine code to create a useable tool path for the FEA code. The next pre-processing function this tool was designed to meet is partitioning and meshing the geometry. Correlating the mesh to the tool path and calculating the times for elements to represent solidified material was also included in the tool. Finally, it was designed to automate the generation of an input file for Abaqus, the FEA code used in this work.

The presented tool was constructed to use open-source software packages, Gmsh, and Python, for most functions [93], [94]. Figure 3.1 shows an overview of the presented framework including the tool, inputs, and outputs. Python was used for the overall framework, interface, and most functions, but the geometry handling and meshing was coded to be carried out with Gmsh. To give geometry and tool path information, the tool was built to use a CAD file in step (.stp) format as well as a tool path specifying the path the moving heat source takes in g-code format. This framework was coded in Python and formulated with modularity in mind. Various sections of the pre-processing tool were broken up into different Python functions to provide users the ability to code their own function to replace the respective part of the tool.

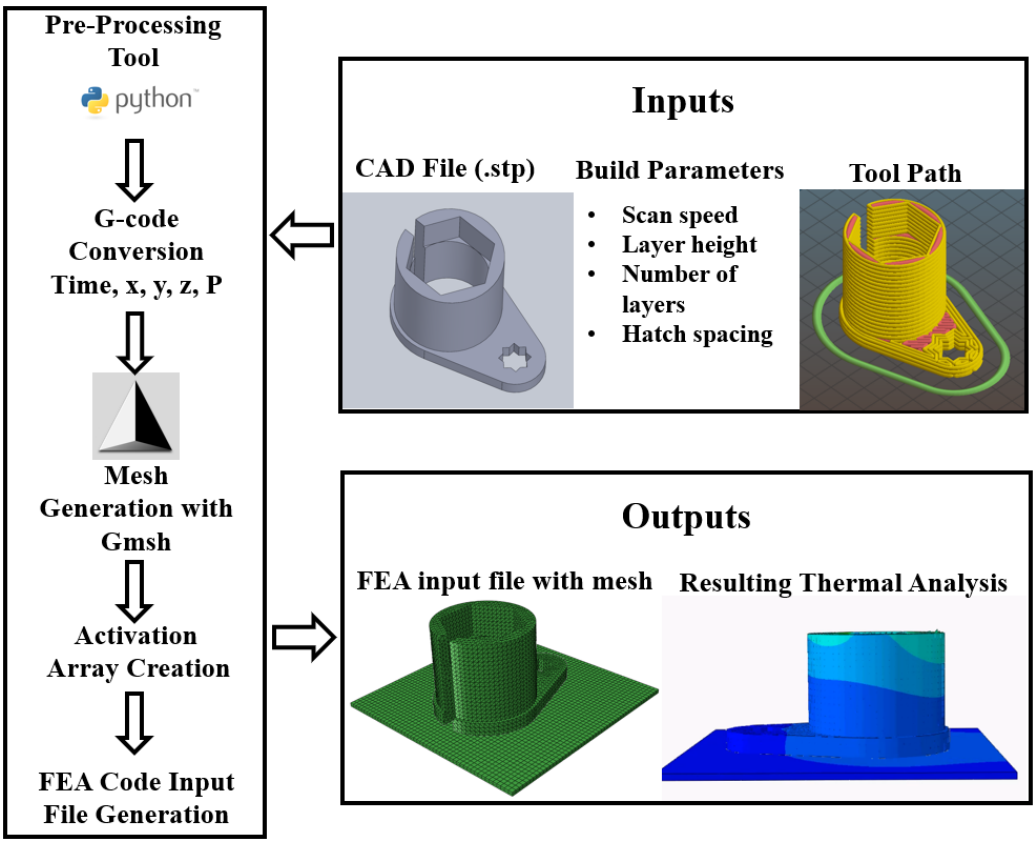

Figure 3.1 Overview of the pre-processing framework.

The Python code that handles the various functions of the pre-processing tool was placed in a file named AM_Preprocessing.py, allowing the user to import the tool as a Python package, and the ability to import any individual function. A summary of the Python functions in the tool are presented in Table 3.1. All inputs for every function are presented and described in Table 3.2

Table 3.1 Summary of the callable Python functions in the pre-processing tool

Function and inputs	Brief description of usage
gen_tool_path(job_name, vel, step, layer_height)	Converts the g-code file into a .csv file containing time, x, y, z at each time step.
gmsh_script(geometry_file, job_name, num_layers, build_dir, sub_height, min_el_len, max_el_len, ref_box)	Creates the Gmsh script to partition and mesh the geometry file.
run_gmsh(job_name, el_order)	Spawns another process to run Gmsh using the script created by *gmsh_script()*
format_inp(job_name, el_order)	Takes the Gmsh generated .inp file, removes any 2D or 1D elements, and changes the element designation to heat transfer elements. Returns the name of the formatted file.
renumber_inp(job_name, inp_file, layer_height)	Takes the re-formatted file from *format_inp()* and sequentially renumbers the elements by layer.
act_creation(job_name, act_d, layer_height)	Creates an activation array file for each layer saying the minimum time at which every element should be active.
inp_sim_format(job_name, layer_height, step)	The final input file formatting. This reformats the input file generated by Abaqus after adding all boundary conditions and step information. It places all necessary keywords and a step for every layer.

Table 3.2 Pre-processing tool inputs

Input name	Description	Example
vel	The velocity of the tool path	vel =12.7 #[mm/s]
step	The time step for the simulation	step = 0.0005 #[seconds]
g_code	Name of the tool path in a g-code format as a string data type	g_code = 'tool_path.gcode'
geometry_file	The step file for the desired geometry as a string data type	geometry_file = 'geom.stp'
num_layers	The number of layers in the desired build defined as a int or float data type	num_layers = 5
build_dir	The direction of the build in the geometry file. This is defined as a Python list with x, y, z directions	build_dir = [0,0,1] (build in the z-direction)
job_name	The desired job name to generate files with as a string data type	job_name = 'build_example'
sub_height	The height of the substrate in the build direction in the geometry file	sub_height = 3.175 #[mm]
layer_height	The height of each layer	layer_height = 0.508 #[mm]
el_order	The order of the elements for the desired mesh. 1=linear elements, 2=quadratic elements	el_order = 2
min_el_len	The minimum side length for elements in the mesh. This will define the mesh density	min_el_len = 0.225 #[mm]
max_el_len	The maximum side length for elements in the mesh. This will decide how much the mesh coarsens away from the part	max_el_len = 1.25 #[mm]
ref_box	This will define the area of the refined mesh around the part as a box. It defines the distance away from the substrate edge that the mesh is refined.	ref_box = 4 #[mm]
act_d	The activation radius around the heat source. This is how far around the laser heat source that elements are activated	act_d = 1.25 #[mm]

3.2 Tool Path Utilization

The heat source path to be used in a simulation was defined through the tool-path input. The pre-processing tool was developed to use g-code, one of the more common machine tool-path formats. Output was formatted as an *m x n* array where *m* is the number of time steps in the simulation and *n* is the number of columns, four. The columns are x-coordinate (x), y-coordinate

(y), z-coordinate (z), and power (P). This section of the tool needed the *vel*, *step*, and *layer_height* inputs as described in Table 3.2. Importing the g-code file into the Python code, each line is saved into an array as strings. Using standard g-code commands, the Python code was built to interpret each line and decide where the heat source would be at each time step location as it loops over the string array. From there, it was coded to write a line with the designated output for every time step of the simulation.

3.3 Mesh Generation

Automated meshing was split into two different Python functions. The first function, *gmsh_script(),* was created to generate a Gmsh script in a .geo file format. The resulting script loads the geometry, locates extremities in the geometry, then it partitions the geometry at the top of the substrate, and partitions the part at each layer. Following the partitioning, functionality was added to the script to define the element lengths based on a box centered around the part. Within the box, the mesh is refined, and outside of the box, the mesh coarsens out to the maximum defined length. The other function, *run_gmsh()*, was created to spawn another process and run Gmsh using the previously created Gmsh script. The part is meshed based on the designated element order and saved to an Abaqus .inp file. The meshing algorithm was designed to take the designated layer height and a desired element size to partition the mesh by layer. Figure 3.3 shows an example of a part using this function. Any meshing tool could be used, if the mesh information can be formatted appropriately for the tool. The pre-processing tool was created to operate with Abaqus input files, .csv, or .txt files of element centroids and numbers in the following format: *element number, x-coordinate, y-coordinate, z-coordinate*.

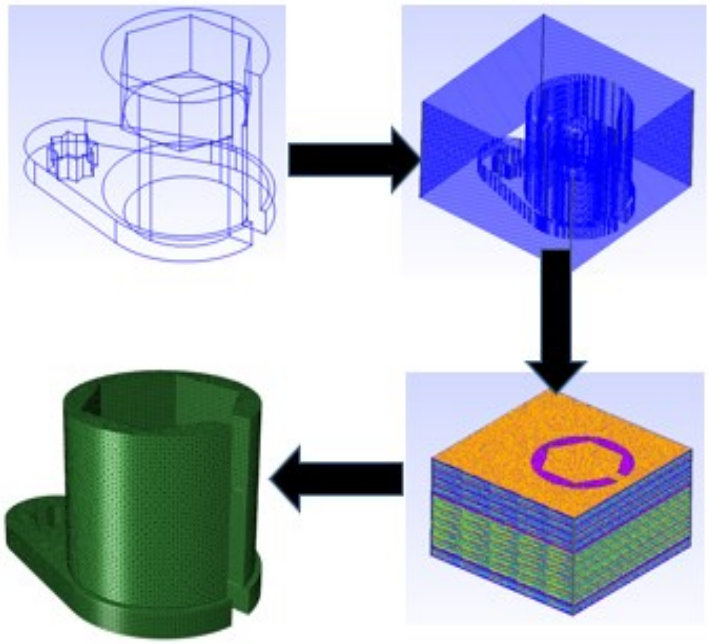

Figure 3.3 A schematic showing the progression from the step file, to the partitioning of the part geometry, then meshing the partitioned geometry, and finally the geometry from the Abaqus input file.

3.4 Activation Determination

The default activation criterion for this framework was based on instantaneous distance from the laser path to any given element. An activation radius was defined for the code to determine the distance from each element's centroid to the current heat source position in the x-y plane at every given time step. From there, this section was coded to take centroids within this defined radius and assign an activation time at the earliest time step it is within range to that element. Figure 3.4 details the activation criterion with a schematic.

The function in the pre-processing tool created to determine activation is named *act_creation()*. First, this function was designed to load the centroids of every element that was created by *renumber_inp()* and the tool path array. Next, the code finds every z-coordinate of each layer, then loops over this array finding every element within the current layer and every time step of the tool path associated with this layer. Within the function a distance calculation

was coded to be carried out between every current element centroid and every relevant timestep. From here, the function was designed to determine the minimum time in which every element centroid is within the desired activation radius from the heat source location, and that time is assigned as the element's activation time. Code was included to save a separate file of elements and activation times for every layer.

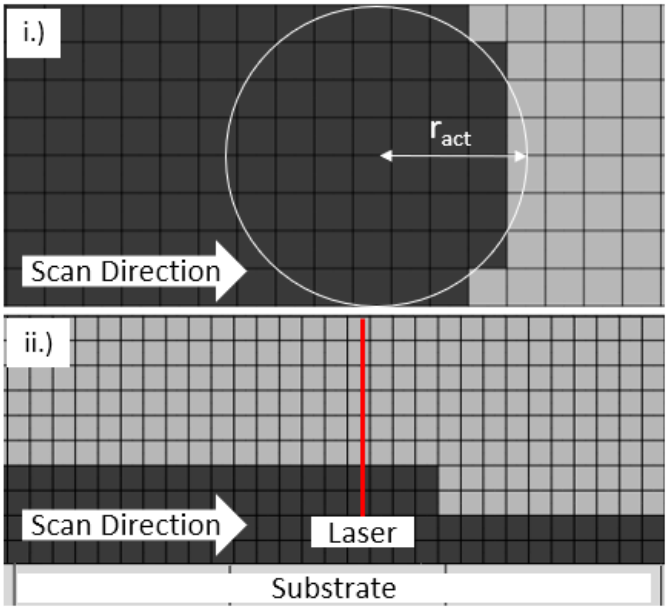

Figure 3.4 Schematic of the element activation criteria used. i.) shows the top of a thin-wall build, and ii.) shows a side view of the progressive activation.

3.5 Input File Generation

Input file generation was handled through multiple steps in the tool throughout pre-processing. The first instance of input file handling was designed to be carried out when the Abaqus input file is originally generated by Gmsh. After this first .inp file is obtained, *format_inp()* was created to be the next function used. This function takes the Gmsh generated file and removes any 2D elements that were created during meshing in Gmsh. From here, *renumber_inp()* was coded to locate all of the element sets, and renumber them based on layer

progression where elements in the substrate start at one, and the highest element number is in the last layer so that Abaqus' UEPACTIVATIONVOL subroutine can read the activation times from multiple files. This function was also created to calculate the centroids for every element to be used in the activation function. Using the .inp file obtained here, the framework was designed to have the user import this into an FEA code, such as Abaqus. There, boundary conditions, loading information, and step data would be specified, and a new input file imported to be used by the final input file formatting function. Finally, *inp_sim_format()* was created to format the Abaqus generated input file. Keywords were added to use Abaqus' element activation utility using the generated activation files and include activation of each layer in the heat transfer step.

CHAPTER IV

CASE STUDY

4.1 Case Study

To illustrate the utility of the pre-processing tool, a case study is detailed here. This case study used a calibrated thermal model of the Laser Engineered Net Shaping (LENS) process to simulate the thermal history of two parts with two different scan strategies. Literature was reviewed to determine which scan strategies to use. Geometries were chosen based on the status of the literature based on what may show varying simulation results. While showcasing the pre-processing tool, this case study also illustrates the effects of geometry and scan strategy on thermal history.

4.2 Geometries and Scan Strategies

The case study consisted of two different build geometries, a cube and a cylinder. Both can be built to similar sizes, and one geometry has four corners, while the other has none. The cube was chosen as it is similar in shape to the commonly simulated thin-wall geometries, but more compact. It should display increased edge-effects compared to the cylinder, where excess heating results at the corners. A cylindrical geometry was chosen to contrast the cube. Presented in Figure 4.1 is a schematic showing each geometry and their dimensions. The substrates were designed to be the same size and have a square face. Each part will be built with four layers spaced 0.508 mm apart. Both geometries were created in Solidworks and exported as step files to be used in the pre-processing tool.

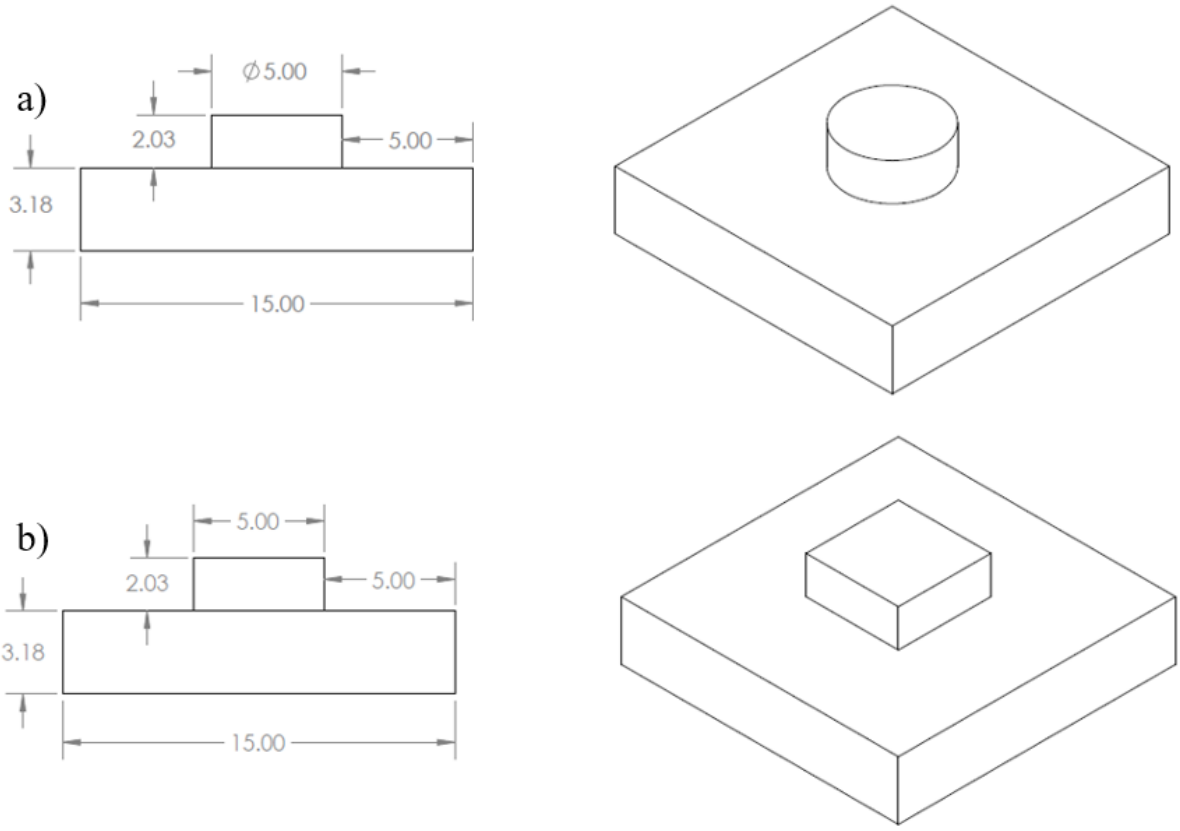

Figure 4.1 Schematic showing a) the cylinder geometry used and b) the cube geometry used in the case study, as well as dimensions in millimeters.

Two commonly used scan strategies were chosen for this case study, a bi-directional pattern and an offset-in pattern. According to several in the literature, there was a reduction in distortion observed from using an offset-in pattern over a bi-directional due to a reduction in thermal gradients [25], [35], [36]. Both scan strategies are simulated with both geometries. A schematic showing each scan strategy with each geometry is presented below, in Figure 4.2. For each case, an outer contour is traced and then the scan strategy is used to fill in the layer. Each layer is identical, without any rotation of the scan strategy. G-code for the scan strategies was

created using Slic3r [95]. Once the g-code was converted to a .csv using the pre-processing tool, adjustments were made by hand in Excel to achieve the final scan strategy.

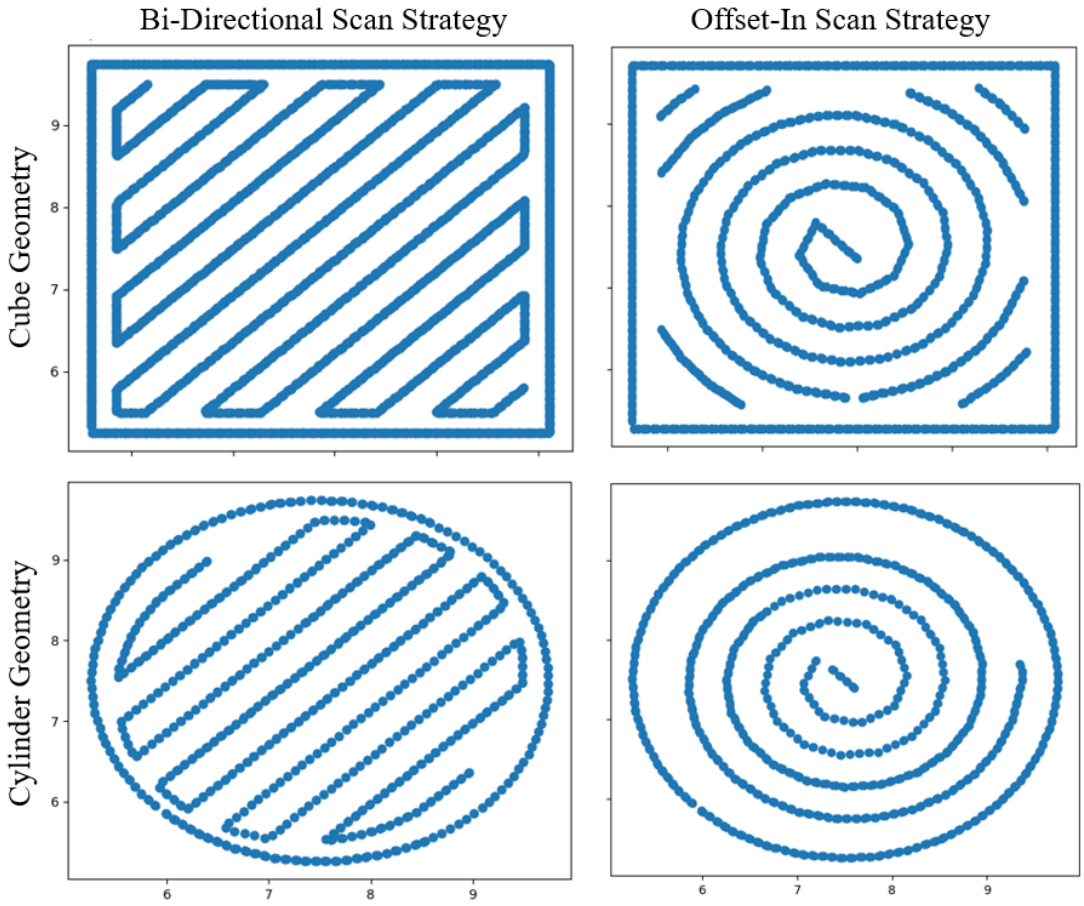

Figure 4.2 Schematic of the two scan strategies on each geometry

4.3 Thermal Analysis

The thermal analysis is conducted through finite element analysis with Abaqus. The work here is based on a thermal model validated with in-situ pyrometer data of a thin-wall build using Ti-6Al-4V [96]. Details of the validation are reviewed in section 4.3. It is carried out as a transient analysis with a moving heat source defined through the Abaqus subroutine, DFLUX. Presented in Eq. 4.1 is the representative energy balance where ρ is the material density, C_p is

specific heat, T is temperature, Q is the supplied heat source, q is the heat flux vector defined by Eq. 4.2, t is time, and spatial coordinates are represented by x, y, and z. In Eq, 4.2, k is the material's thermal conductivity. The volumetric heat source applied using Dflux, Q in Eq 4.1, is Goldak's Ellipsoidal heat source presented in Eq 2.1. Values used for the parameters in Eq 2.1 were obtained through calibration to the in-situ pyrometer data and are presented in Table 4.1.

$$\rho C_p \frac{dT}{dt} = Q(x,y,z,t) - q(x,y,z,t) \tag{4.1}$$

$$q = -k\nabla T \tag{4.2}$$

Table 4.1 Goldak equation parameters

Parameter	**Value**
Efficiency, η (%)	37
Gaussian distribution tuning parameter, σ	3.0
Depth, d (mm)	0.54
Laser spot size, r (mm)	0.89

The thermal analysis must consider boundary conditions present during the LENS process. These boundary conditions include convection and radiation form the laser heat source. While most heat dissipates through conduction, there is a non-negligible amount of heat lost through convection from the gas that carries the blown powder. Newton's Law of cooling, presented in Eq 4.3, accounts for convection losses in the analysis. For this problem, the convection coefficient, h, is $30\ W/m^2K$ on the top surface to simulate forced convection from shielding gas, and $10\ W/m^2K$ everywhere else for free convection.

$$q_{conv} = h\left(T_{surface} - T_{\infty}\right) \tag{4.3}$$

Heat loss due to radiation is accounted for through the Stefan-Boltzmann Law, shown in Eq 4.4. In this equation, $q_{radiation}$ is the heat loss due, σ_{SB} is Stefan-Boltzmann's constant, and ε is the emissivity of Ti-6Al-4V defined as 0.54.

$$q_{radiation} = \sigma_{SB}\varepsilon\left(T^4{}_{surface} - T_\infty^4\right) \tag{4.4}$$

With temperatures ranging from an ambient temperature of 310 K to above molten (1877 K), temperature dependent thermal properties are needed. Temperature dependent density, thermal conductivity, and specific heat values, shown in Figure 4.3, are taken from Mills [97]. The discontinuities shown in Figure 4.3 occurs at two phase transition temperatures. The beta transus for Ti-64 is at 995 °C and this is where the HCP alpha phase transforms in the BCC beta phase. The other discontinuity is at the liquidus temperature, 1660 °C, where the material is assumed to be completely liquid.

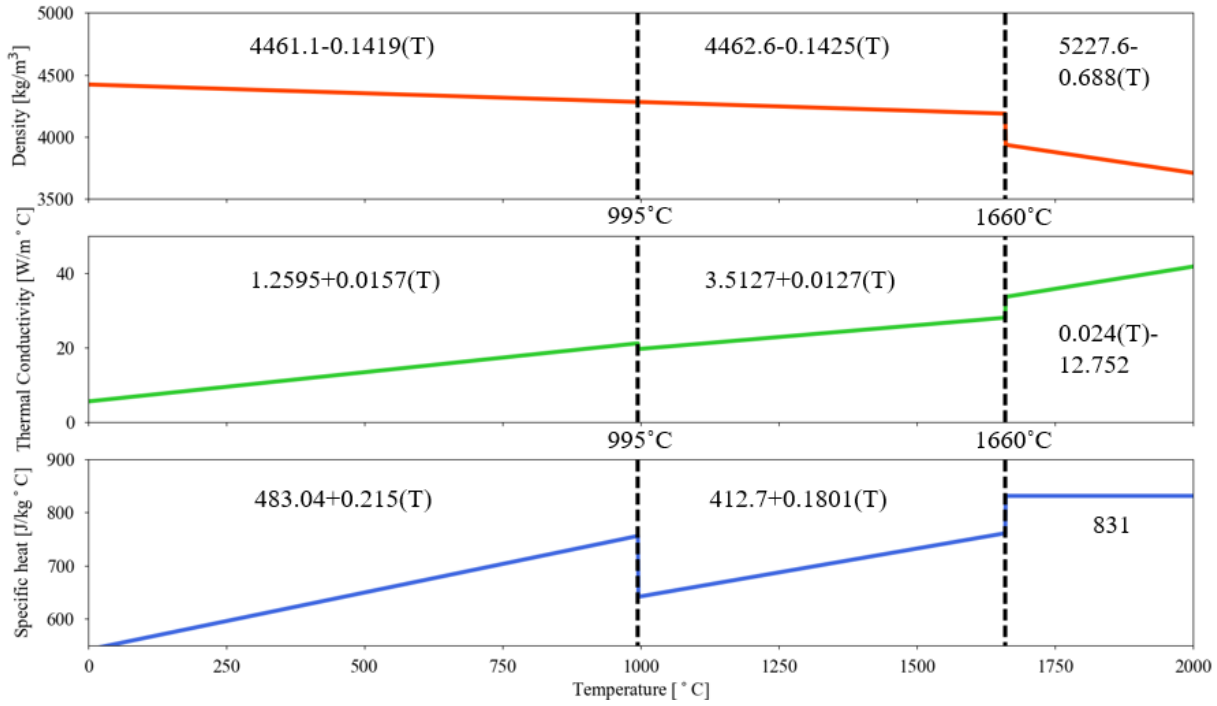

Figure 4.3 Temperature dependent material properties for Ti-6Al-4V used in the simulations

4.4 Thermal Model Validation

The validation simulation was carried out to mimic an experiment presented in Marshall et al. and using the in-situ pyrometer data collected during that build using Abaqus finite element software [98]. A thin-wall, single deposition track geometry was built using the processing parameters presented below in Table 4.2. Pyrometer images consisted of a 752 x 480 matrix of temperature measurements encompassing the melt pool, taken using a Stratonics dual-wave pyrometer. With a capture frequency ranging from 4-7 Hz, there were approximately 25 of these images per layer, but the first few images of a layer did not contain a melt pool. The estimated error of the temperature measurements is taken from Kriczky et al. as +/- 12.5 °C [99].

Table 4.2 Validation simulation processing parameters

Parameter	Value
Laser Power (W)	290
Laser Scan Speed (mm/s)	12.7
Layer Height (mm)	0.508
Layer Width (mm)	1.78
Dwell Time (s)	2.0

The model predicts the first layer of the build with approximately 1.51 % error at the maximum temperature and 15.87 % error to the melt pool diameter. Figure 4.4 shows an image of the simulation and pyrometer taken at similar points during the first layer deposition with all values removed that are outside of the pyrometer calibration range. Furthermore, Figure 4.5 displays the temperature profile taken down the center of the melt pool in the build direction from one frame of the simulation in the middle of the build. This figure is plotted against the range of pyrometer profiles during the steady-state region of the first layer. The average percent error for the simulation along this center profile is 2.4 %.

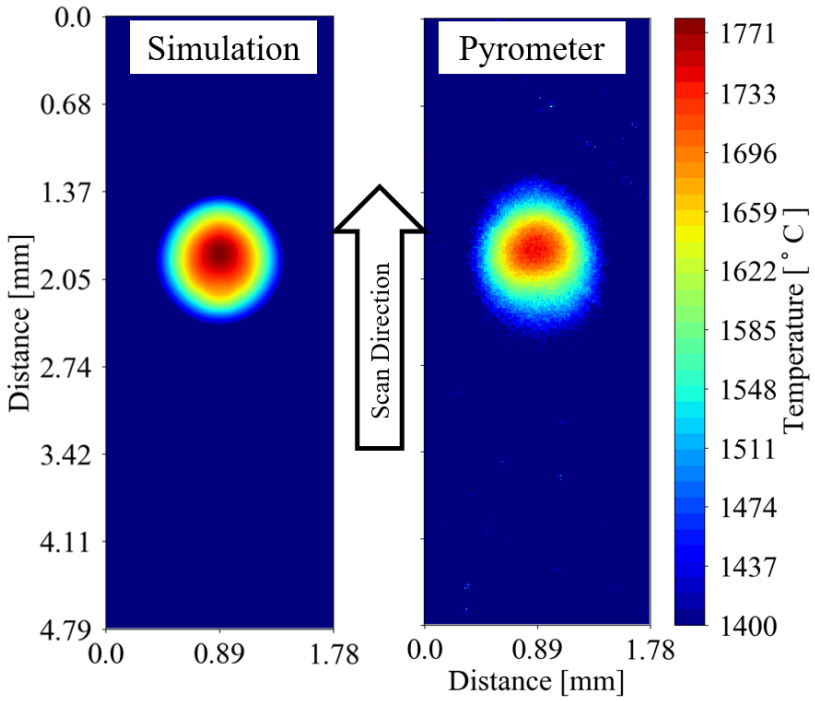

Figure 4.4 Images comparing raw Abaqus output, interpolated values, and a pyrometer image for similar times during the build.

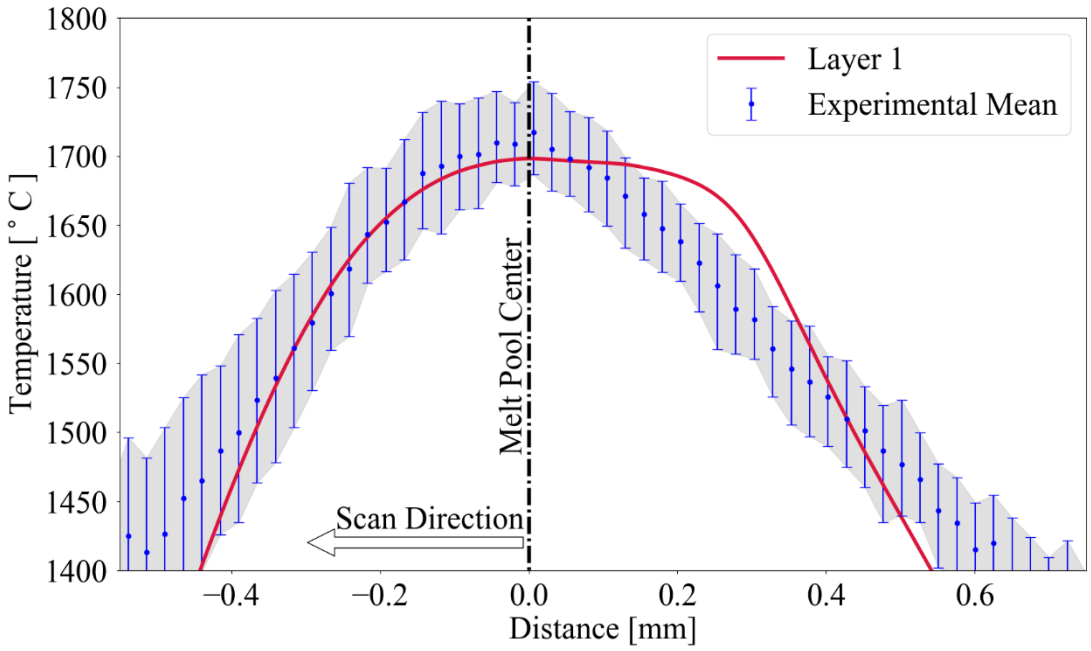

Figure 4.5 Temperature profile down the center of the melt pool for layer one of the validation simulation compared to the experimental mean of the pyrometer data for layer one.

4.5 Simulation Set-up

The case study Abaqus simulations were set up with parameters similar to those used by the validation simulation. Table 4.2 details the build parameters used in the case study simulations. Using the pre-processing tool, the .stp files generated through Solidworks were meshed with Gmsh quadratic tetrahedral elements. The Abaqus element designation is DC3D10 heat transfer elements. Mesh refinement was conducted around the part 4 mm away from the edges of the substrate and one layer height below the part. The most refined area was designated to have an element side length of 0.15 mm and this coarsens out to a size of 1.25 mm at the substrate edges. A view of the mesh showing the layer and substrate partitioning using the Gmsh GUI is shown in Figure 4.7. Table 4.3 gives a breakdown of the number of elements in each model. Using this meshing, the activation radius, as denoted in Figure 3.4, that was used is 1.5

mm. This is a large radius and was mostly chosen to ease in convergence during the simulations. The time step used was 0.0005 s.

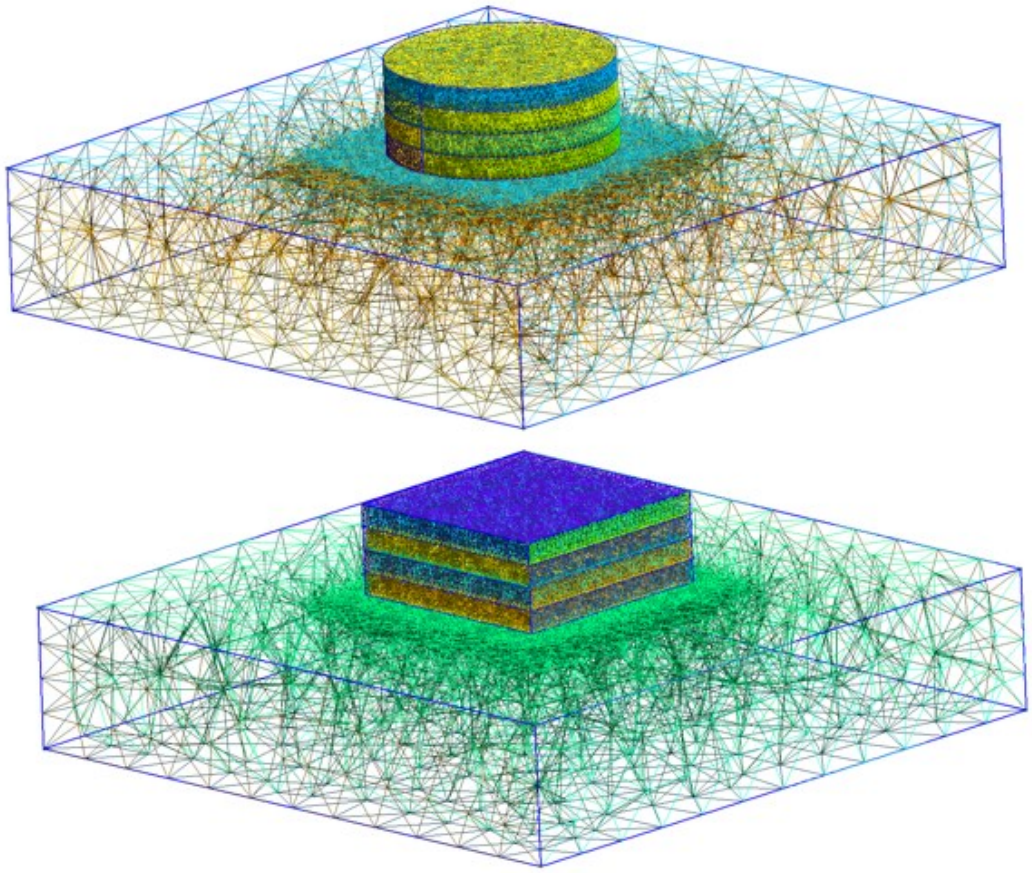

Figure 4.6 Final meshes for the cube and cylinder geometries created with Gmsh.

Table 4.3 Element counts for different regions in each geometry and the total number of elements.

Region	**Cylinder**	**Cube**
Substrate	37,527	37,797
Layer 1	16,254	20,703
Layer 2	16,164	20,548
Layer 3	16,216	20,768
Layer 4	16,313	20,775
Total	102,474	120,591

CHAPTER V

RESULTS

5.1 Case Study Results

Simulation results for the four cases are presented here. Temperature profiles of the top surface of the build for the end of layer one is shown in Figure 5.1. In Figure 5.2, the temperature profiles for the end of layer 4 is shown.

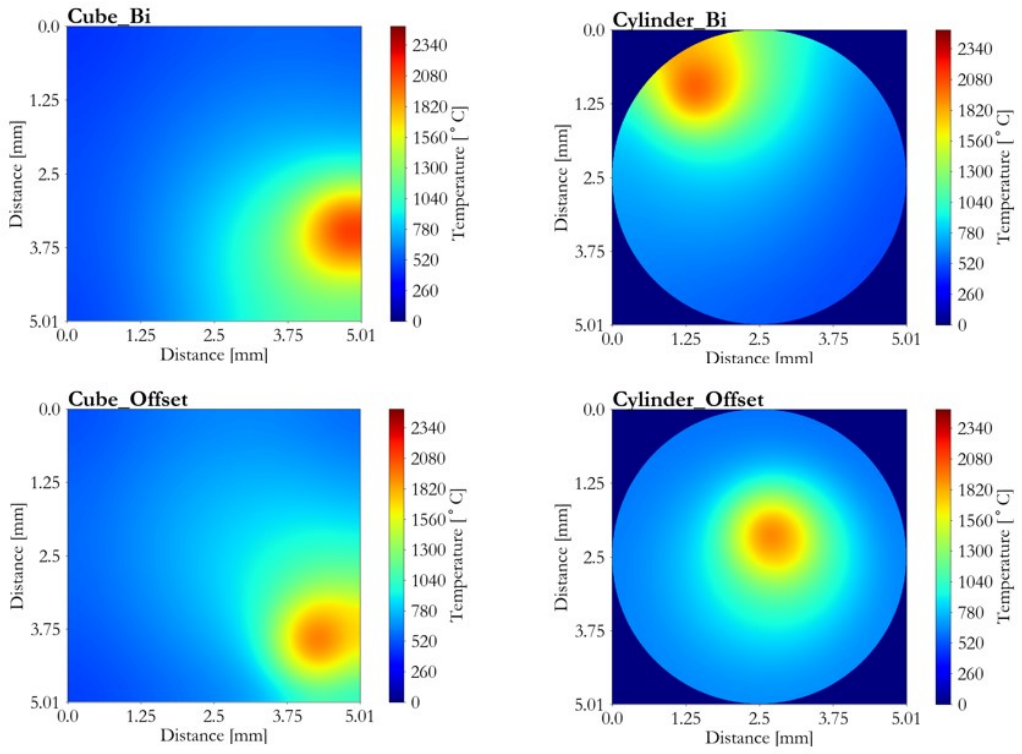

Figure 5.1 Temperature profile at the end of layer one for each case.

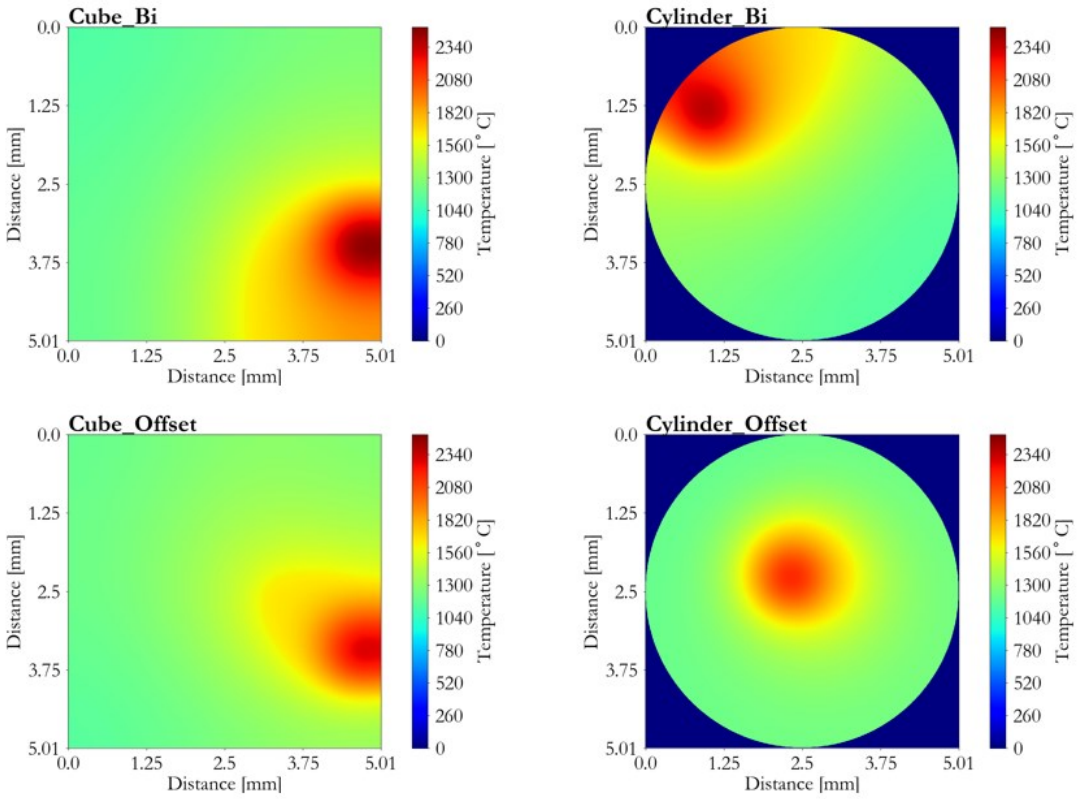

Figure 5.2 Temperature profile at the end of layer four for each case.

There is a noticeable difference between the temperature history from each case. Table 5.1 presents the maximum temperature shown by each case for each layer. It is important to note that the cube geometry contains more volume than the cylinder and required longer scan times. Likewise, the bi-directional scan strategy required longer build times.

Table 5.1 Maximum temperature in each layer for each build case.

Layer	Cube Bi	Cube Offset	Cylinder Bi	Cylinder Offset
Layer 1	2112 °C	1930 °C	2008 °C	1904 °C
Layer 2	2305 °C	2071 °C	2188 °C	1990 °C
Layer 3	2403 °C	2199 °C	2263 °C	2067 °C
Layer 4	2469 °C	2294 °C	2410 °C	2166 °C

To further analyze the temperature evolution over the build time, the maximum temperature across the build is given in Figure 5.3.

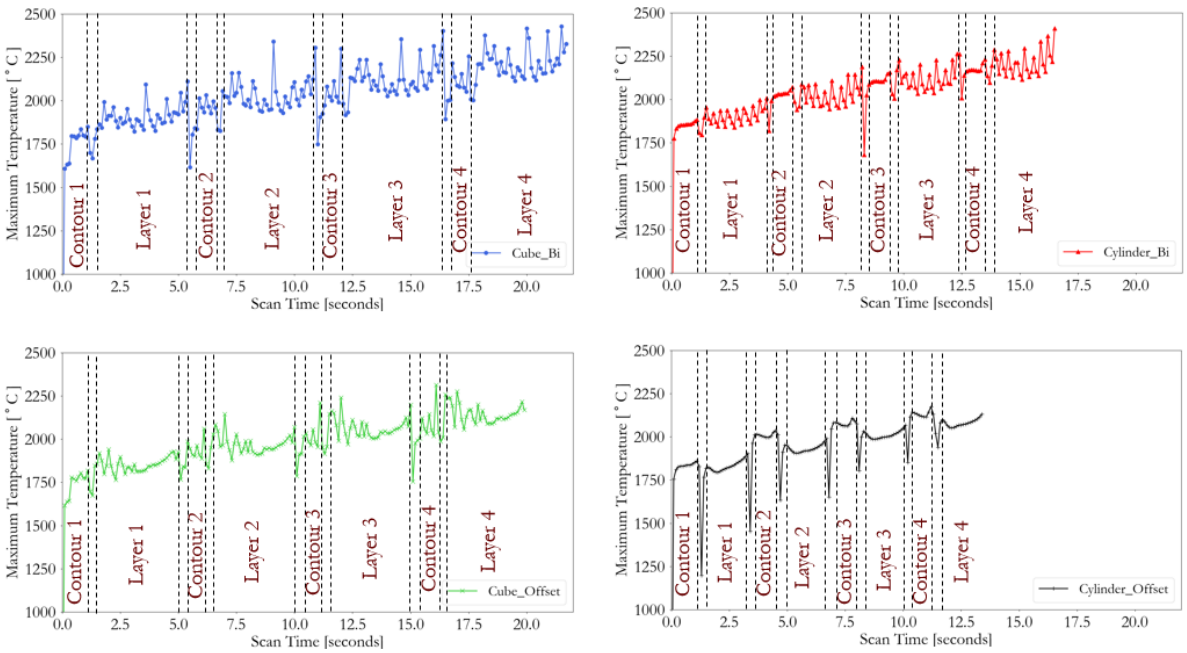

Figure 5.3 Maximum temperature throughout the build for each case.

To compare the different geometries, the maximum temperature is plotted in Figure 5.4 for each geometry with the same scan strategy. Likewise, Figure 5.5 plots the maximum temperature for each scan strategy with the same geometry to contrast the different scan strategies.

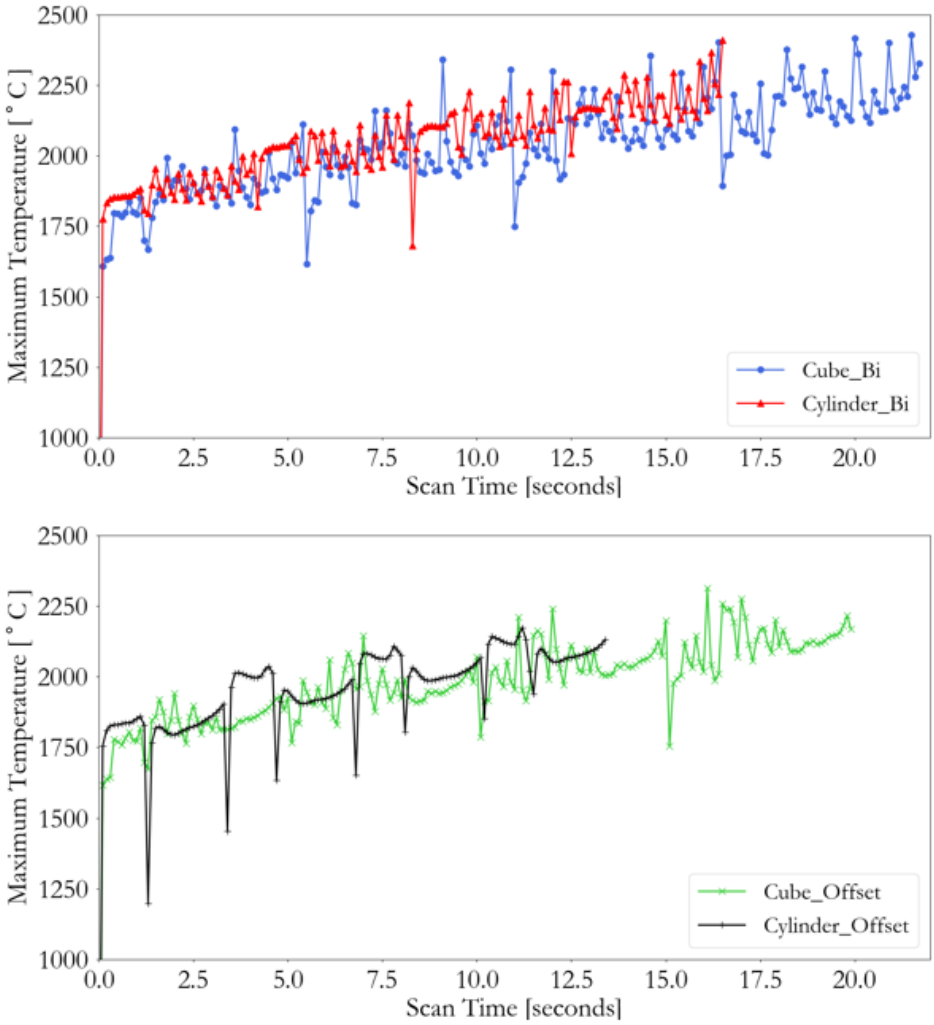

Figure 5.4 Maximum temperature throughout the build comparing different geometries with the same scan strategies.

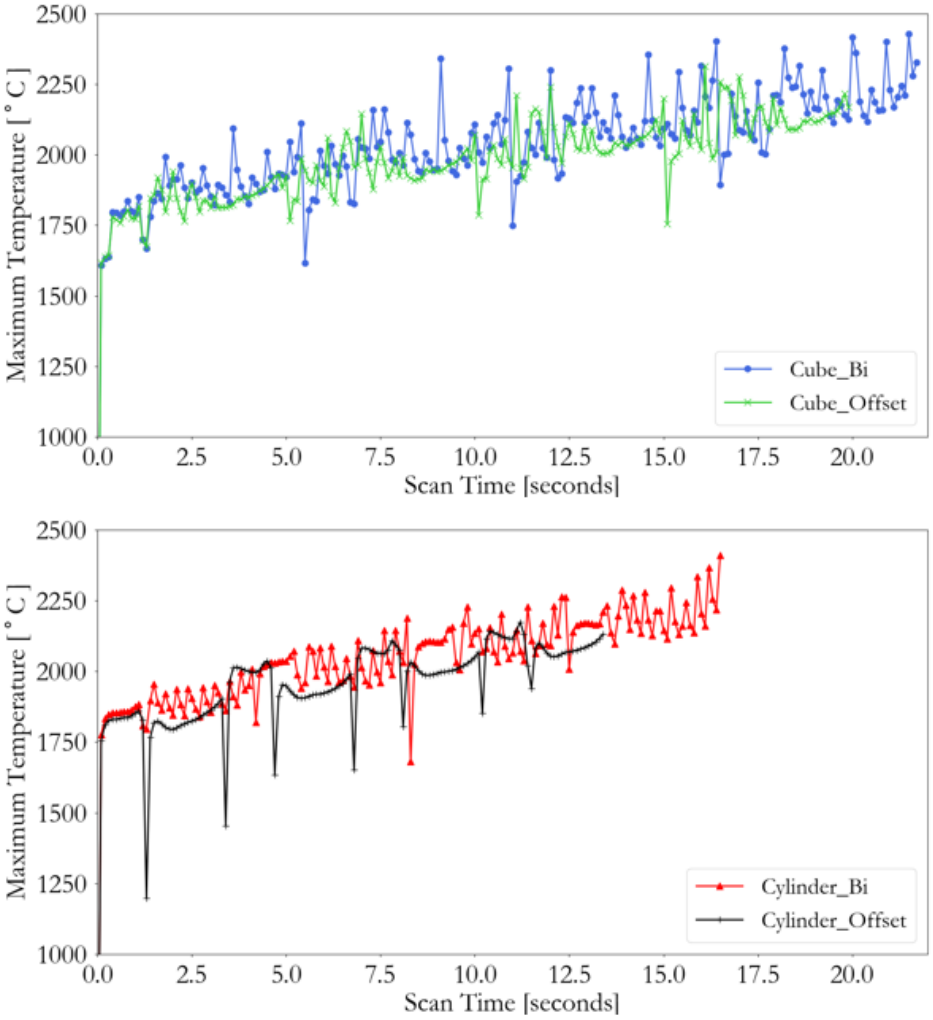

Figure 5.5 Maximum temperature throughout the build comparing different scan strategies with the same geometry.

Thermal gradients at the end of each layer were calculated between every node in the simulations. Presented in Table 5.2 are the maximum thermal gradient for each layer for each case.

Table 5.2 Maximum thermal gradient (°C/mm) at the end of each layer for each build case.

Layer	Cube Bi	Cube Offset	Cylinder Bi	Cylinder Offset
Layer 1	1399	1330	1287	1332
Layer 2	991.2	1269	1209	1210
Layer 3	954.9	1250	1207	1182
Layer 4	1085	1176	1102	986.6

During the simulations running, the cylinder offset case had the easiest time of converging, with the cube offset being second. However, to get the simulations to run through four full layers, the Abaqus convergence tolerances were increased. The ratio tolerance of the largest residual heat flux to the average flux norm was increased from $5x10^{-3}$ to 2.0. The alternative ratio was changed from $2x10^{-2}$ to 4.0, and the maximum number of iterations before the alternative is used was decreased form 9 to 5. Also, the convergence criteria for the ratio of the largest temperature solution correction to the largest incremental temperature value was increased form $1x10^{-2}$ to 1.0.

5.2 Pre-Processing Tool Results

The pre-processing tool ran successfully for the geometries used here. A summary of the time taken to perform each major pre-processing section for running the AM simulations is presented in Table 5.1. The tool path time reported is only for offset scan strategies for each geometry. Likewise, the activation creation times are only for the offset scan strategies. These times are dependent on the number of elements in the mesh as well as the time step being used. It is important to note that these times do not include the time to add boundary and loading conditions through the Abaqus GUI.

Table 5.3 Time measurements for major sections of the pre-processing tool for each geometry.

Function	**Cylinder**	**Cube**
Tool Path (s)	1.25	1.51
Meshing (s)	9.75	13.49
Activation creation (s)	29.7	34.65
Input file formatting (s)	23.87	26.59
Total (s)	64.54	76.24

The presented pre-processing tool was able to accomplish all tasks in less than 1.5 minutes. This is significantly faster than if these tasks were to be performed by hand. With 102,474 elements for the cylinder and 120,591 elements for the cube, assigning an activation time for each would not be feasible if done by hand. Partitioning by layer and created a refined region would be much slower if done by hand than the sub 20 second times presented here. This is compounded by the ability to quickly create multiple meshes for a mesh convergence study simultaneously by using a loop in Python and looping over the meshing utilities.

From the case study it can be seen that for the offset scan strategy, as shown in Figures 5.1 and 5.2, the hottest area of the melt pool is smaller than for the bi-directional strategy. All of the maximum temperature plots show significantly less temperature fluctuations for the offset strategies than for the bi-directional. This is possibly why those in the literature experienced less distortion from an offset scan strategy than a bi-directional strategy. The maximum temperatures presented in Table 5.1 show a temperature of 182 °C less in layer one and 175 °C in layer four for the offset strategy than the bi-directional in the cube geometry. The cylinder geometry experienced 104 °C and 244 °C less for layers one and , respectively from the offset to the bi-directional geometry. Some of this could be from the longer scan times used by Slic3r for the bi-directional scan strategies.

Shown in the maximum temperature plots, it is apparent that there are also more temperature spikes from the cube geometry compared to the cylinder geometry, even for the same scan strategy. These extra temperature spikes is probably from edge effects, especially at the corners of the cube. Table 5.1 shows an increase in maximum temperatures for each layer for the cube geometry, compared to the cylinder. For the bi-directional scan strategy, the cube experienced a 104 °C and 59 °C higher temperature for layers one and four, respectively. The

offset scan strategy showed a higher temperature in the cube of 26 °C and 128 °C for layers one and two, respectively. However, the cube has more volume than the cylinder and required longer scan times to build.

The thermal gradients for each case show a decrease as the build progresses, except for the Cube bi case which has a spike at the end of the last layer. Decreasing thermal gradients throughout the build is expected, as the gradients would drop as the part and substrate heat up. In the Cylinder offset case, the lowest final thermal gradient is experienced, whereas the highest gradient is seen in the Cube offset case.

CHAPTER VI

CONCLUSIONS AND FUTURE WORK

This thesis has presented the development of a pre-processing tool that can provide significant time savings by meshing, partitioning, and setting up activation times for each element for finite element simulations of AM processes. The case study conducted here to showcase this pre-processing tool has shown that more temperature spikes are experienced for a bi-directional scan strategy over an offset scan strategy. Likewise, a cube geometry experiences more temperature fluctuations compared to a cylindrical geometry and this is likely due to increased edge effects.

The code presented here could be improved through several avenues, such as improving meshing capabilities by allowing the use of hexahedral elements. Currently it is limited to meshing with tetrahedral elements. Allowing a more gradual mesh refinement region would help convergence and allow better applicability to more complex part geometries. Currently, the user has to go into the used finite element code to add boundary conditions. Including the ability to add boundary conditions through the tool would provide significant time savings. Including a command line-based slicing software that could be run by the tool for common scan strategies would reduce one of the most time-consuming inputs to the tool. To make the tool entireling inputs to the tool. To make the tool entirely open-source in every aspect, functionality with an open-source FEA code would be a necessity. One of the most important next steps for this work would be to run accurate FEA simulations of an even more complex geometry.

REFERENCES

[1] M. M. Francois *et al.*, "Modeling of additive manufacturing processes for metals: Challenges and opportunities," *Current Opinion in Solid State and Materials Science*, vol. 21, no. 4, pp. 198–206, Aug. 2017.

[2] C. H. Fu and Y. B. Guo, "3-Dimensional Finite Element Modeling of Selective Laser Melting TI-6AL-4V Alloy," p. 16.

[3] J. Irwin, E. W. Reutzel, P. Michaleris, J. Keist, and A. R. Nassar, "Predicting Microstructure From Thermal History During Additive Manufacturing for Ti-6Al-4V," *J. Manuf. Sci. Eng*, vol. 138, no. 11, p. 111007, Jun. 2016.

[4] S. Sahoo and K. Chou, "Phase-field simulation of microstructure evolution of Ti–6Al–4V in electron beam additive manufacturing process," *Additive Manufacturing*, vol. 9, pp. 14–24, Jan. 2016.

[5] T. M. Rodgers, J. D. Madison, and V. Tikare, "Simulation of metal additive manufacturing microstructures using kinetic Monte Carlo," *Computational Materials Science*, vol. 135, pp. 78–89, Jul. 2017.

[6] A. Zinoviev, O. Zinovieva, V. Ploshikhin, V. Romanova, and R. Balokhonov, "Evolution of grain structure during laser additive manufacturing. Simulation by a cellular automata method," *Materials & Design*, vol. 106, pp. 321–329, Sep. 2016.

[7] S. A. Khairallah, A. T. Anderson, A. Rubenchik, and W. E. King, "Laser powder-bed fusion additive manufacturing: Physics of complex melt flow and formation mechanisms of pores, spatter, and denudation zones," *Acta Materialia*, vol. 108, pp. 36–45, 2016.

[8] N. Raghavan *et al.*, "Numerical modeling of heat-transfer and the influence of process parameters on tailoring the grain morphology of IN718 in electron beam additive manufacturing," *Acta Materialia*, vol. 112, pp. 303–314, Jun. 2016.

[9] K. L. Johnson *et al.*, "Simulation and experimental comparison of the thermo-mechanical history and 3D microstructure evolution of 304L stainless steel tubes manufactured using LENS," *Computational Mechanics*, vol. 61, no. 5, pp. 559–574, May 2018.

[10] J. C. Heigel, P. Michaleris, and E. W. Reutzel, "Thermo-mechanical model development and validation of directed energy deposition additive manufacturing of Ti–6Al–4V," *Additive Manufacturing*, vol. 5, pp. 9–19, Jan. 2015.

[11] E. R. Denlinger and J. Irwin, “Thermomechanical Modeling of Additive Manufacturing Large Parts,” vol. 136, no. December 2014, pp. 1–8, 2018.

[12] Q. Yang, P. Zhang, L. Cheng, Z. Min, M. Chyu, and A. C. To, “Finite element modeling and validation of thermomechanical behavior of Ti-6Al-4V in directed energy deposition additive manufacturing,” *Additive Manufacturing*, vol. 12, pp. 169–177, 2016.

[13] N. E. Hodge, R. M. Ferencz, and J. M. Solberg, “Implementation of a thermomechanical model for the simulation of selective laser melting,” *Comput Mech*, vol. 54, no. 1, pp. 33–51, Jul. 2014.

[14] L. Bian, S. M. Thompson, and N. Shamsaei, “Mechanical Properties and Microstructural Features of Direct Laser-Deposited Ti-6Al-4V,” *JOM*, vol. 67, no. 3, pp. 629–638, Mar. 2015.

[15] P. Mercelis and J. Kruth, “Residual stresses in selective laser sintering and selective laser melting,” *Rapid Prototyping Journal*, vol. 12, no. 5, pp. 254–265, 2006.

[16] W. E. Frazier, “Metal additive manufacturing: A review,” *Journal of Materials Engineering and Performance*, vol. 23, no. 6, pp. 1917–1928, 2014.

[17] Y. Huang, M. C. Leu, J. Mazumder, and A. Donmez, “Additive Manufacturing: Current State, Future Potential, Gaps and Needs, and Recommendations,” *Journal of Manufacturing Science and Engineering*, vol. 137, no. February 2015, pp. 1–10, 2015.

[18] S. A. M. Tofail, E. P. Koumoulos, A. Bandyopadhyay, S. Bose, L. O’Donoghue, and C. Charitidis, “Additive manufacturing: scientific and technological challenges, market uptake and opportunities,” *Materials Today*, vol. 21, no. 1, pp. 22–37, Jan. 2018.

[19] J. Alcisto *et al.*, “Tensile Properties and Microstructures of Laser-Formed Ti-6Al-4V,” vol. 20, no. March, pp. 203–212, 2011.

[20] T. Wohlers and T. Gornet, “History of additive manufacturing,” p. 38, 2016.

[21] L. E. Murr *et al.*, “Metal Fabrication by Additive Manufacturing Using Laser and Electron Beam Melting Technologies,” *Journal of Materials Science and Technology*, vol. 28, no. 1, pp. 1–14, 2012.

[22] L. Thijs, F. Verhaeghe, T. Craeghs, J. Van Humbeeck, and J. P. Kruth, “A study of the microstructural evolution during selective laser melting of Ti-6Al-4V,” *Acta Materialia*, vol. 58, no. 9, pp. 3303–3312, 2010.

[23] L. Bian, S. M. Thompson, and N. Shamsaei, “Mechanical Properties and Microstructural Features of Direct Laser-Deposited Ti-6Al-4V,” *JOM*. 2015.

[24] A. B. Spierings and G. Levy, “Comparison of density of stainless steel 316L parts produced with selective laser melting using different powder grades,” *Solid Freeform Fabrication Proceedings*, pp. 342–353, 2009.

[25] N. Shamsaei, A. Yadollahi, L. Bian, and S. M. Thompson, “An overview of Direct Laser Deposition for additive manufacturing; Part II: Mechanical behavior, process parameter optimization and control,” *Additive Manufacturing*, 2015.

[26] S. M. Thompson, L. Bian, N. Shamsaei, and A. Yadollahi, “An overview of Direct Laser Deposition for additive manufacturing; Part I: Transport phenomena, modeling and diagnostics,” *Additive Manufacturing*. 2015.

[27] W. Hofmeister and M. Griffith, “Solidification in direct metal deposition by LENS processing,” *Jom*, vol. 53, no. 9, pp. 30–34, 2001.

[28] L. Wang, S. D. Felicelli, and J. E. Craig, “Experimental and numerical study of the LENS rapid fabrication process,” *Journal of Manufacturing Science and Engineering*, vol. 131, no. 4, p. 041019, 2009.

[29] P. A. Kobryn and S. L. Semiatin, “Microstructure and texture evolution during solidification processing of Ti–6Al–4V,” *Journal of Materials Processing Technology*, vol. 135, no. 2–3, pp. 330–339, 2003.

[30] S. Bontha, N. W. Klingbeil, P. A. Kobryn, and H. L. Fraser, “Thermal process maps for predicting solidification microstructure in laser fabrication of thin-wall structures,” *Journal of Materials Processing Technology*, vol. 178, no. 1–3, pp. 135–142, 2006.

[31] M. M. Francois *et al.*, “Modeling of additive manufacturing processes for metals: Challenges and opportunities,” *Current Opinion in Solid State and Materials Science*, vol. 21, no. 4, pp. 198–206, Aug. 2017.

[32] A. M. Beese and B. E. Carroll, “Review of Mechanical Properties of Ti-6Al-4V Made by Laser- Based Additive Manufacturing Using Powder Feedstock,” vol. 68, no. 3, pp. 724–734, 2016.

[33] P. Li, D. H. Warner, A. Fatemi, and N. Phan, “Critical assessment of the fatigue performance of additively manufactured Ti–6Al–4V and perspective for future research,” *International Journal of Fatigue*, vol. 85, pp. 130–143, Apr. 2016.

[34] N. T. Aboulkhair, N. M. Everitt, I. Ashcroft, and C. Tuck, “Reducing porosity in AlSi10Mg parts processed by selective laser melting,” *Additive Manufacturing*, vol. 1, pp. 77–86, 2014.

[35] K. Dai and L. Shaw, “Distortion minimization of laser-processed components through control of laser scanning patterns,” *Rapid Prototyping Journal*, vol. 8, no. 5, pp. 270–276, 2002.

[36] J. Yu *et al.*, "Influence of laser deposition patterns on part distortion, interior quality and mechanical properties by laser solid forming (LSF)," *Materials Science and Engineering: A*, vol. 528, no. 3, pp. 1094–1104, Jan. 2011.

[37] A. H. Nickel, D. M. Barnett, and F. B. Prinz, "Thermal stresses and deposition patterns in layered manufacturing," *Materials Science and Engineering: A*, vol. 317, no. 1–2, pp. 59–64, Oct. 2001.

[38] A. A. Antonysamy, J. Meyer, and P. B. Prangnell, "Effect of build geometry on the β-grain structure and texture in additive manufacture of Ti6Al4V by selective electron beam melting," *Materials Characterization*, vol. 84, pp. 153–168, Oct. 2013.

[39] L. A. Parry, I. A. Ashcroft, and R. D. Wildman, "Geometrical effects on residual stress in selective laser melting," *Additive Manufacturing*, vol. 25, pp. 166–175, Jan. 2019.

[40] F. Vásquez, J. A. Ramos-Grez, and M. Walczak, "Multiphysics simulation of laser-Material interaction during laser powder depositon," *International Journal of Advanced Manufacturing Technology*, vol. 59, no. 9–12, pp. 1037–1045, 2012.

[41] A. J. Pinkerton and L. Li, "Modelling the geometry of a moving laser melt pool and deposition track via energy and mass balances," *J. Phys. D: Appl. Phys.*, vol. 37, no. 3704, pp. 1885–1895, 2004.

[42] W. Liu and J. N. Dupont, "In-situ reactive processing of nickel aluminides by laser-engineered net shaping," *Metall and Mat Trans A*, vol. 34, no. 11, pp. 2633–2641, Nov. 2003.

[43] P. A. Kobryn and S. L. Semiatin, "Mechanical properties of laser-deposited Ti-6Al-4V," *Solid Freeform Fabrication Proceedings*, pp. 6–8, 2001.

[44] G. B. Olson, "Computational Design of Hierarchically Structured Materials," *Science*, vol. 277, no. 5330, pp. 1237–1242, Aug. 1997.

[45] G. E. Dieter, *Mechanical Metallurgy*, Third Edit. McGraw-Hill, 1986.

[46] W. Chen, C. J. Boehlert, J. Y. Howe, and E. A. Payzant, "Elevated-temperature mechanical behavior of As-cast and wrought Ti-6Al-4V-1B," *Metallurgical and Materials Transactions A: Physical Metallurgy and Materials Science*, vol. 42, no. 10, pp. 3046–3061, 2011.

[47] Y. Wang, S. Zhang, X. Tian, and H. Wang, "High-cycle fatigue crack initiation and propagation in laser melting deposited TC18 titanium alloy," *International Journal of Minerals, Metallurgy, and Materials*, vol. 20, no. 7, pp. 665–670, 2013.

[48] X. Tan *et al.*, "Graded microstructure and mechanical properties of additive manufactured Ti–6Al–4V via electron beam melting," *Acta Materialia*, vol. 97, pp. 1–16, Sep. 2015.

[49] Z. Wang, T. A. Palmer, and A. M. Beese, "Effect of processing parameters on microstructure and tensile properties of austenitic stainless steel 304L made by directed energy deposition additive manufacturing," *Acta Materialia*, vol. 110, pp. 226–235, May 2016.

[50] I. J. Polmear, *Light Alloys Metallurgy of the Light Metals*. 1989.

[51] P. Heinl, L. Müller, C. Körner, R. F. Singer, and F. A. Müller, "Cellular Ti-6Al-4V structures with interconnected macro porosity for bone implants fabricated by selective electron beam melting," *Acta Biomaterialia*, vol. 4, no. 5, pp. 1536–1544, 2008.

[52] T. F. Ã, B. Hoffschmidt, R. Pitz-paal, O. Reutter, and P. Rietbrock, "Porous materials as open volumetric solar receivers : Experimental determination of thermophysical and heat transfer properties," vol. 29, pp. 823–833, 2004.

[53] L. Wang, P. Pratt, S. Felicelli, H. Kadiri, and P. Wang, "Experimental Analysis of Porosity Formation in Laser-Assisted Powder Deposition Process," vol. 1, pp. 389–396, 2009.

[54] G. D. Scott and D. M. Kilgour, "The density of random close packing of spheres," *Journal of Physics D: Applied Physics*, vol. 2, no. 6, pp. 863–866, 2002.

[55] A. B. Spierings, N. Herres, and G. Levy, "Influence of the particle size distribution on surface quality and mechanical properties in AM steel parts," *Rapid Prototyping Journal*, vol. 17, no. 3, pp. 195–202, 2011.

[56] D. F. Susan, J. D. Puskar, J. A. Brooks, and C. V. Robino, "Quantitative characterization of porosity in stainless steel LENS powders and deposits," *Materials Characterization*, vol. 57, no. 1, pp. 36–43, 2006.

[57] M. N. Ahsan, A. J. Pinkerton, R. J. Moat, and J. Shackleton, "A comparative study of laser direct metal deposition characteristics using gas and plasma-atomized Ti-6Al-4V powders," *Materials Science and Engineering A*, vol. 528, no. 25–26, pp. 7648–7657, 2011.

[58] T. Vilaro, C. Colin, and J. D. Bartout, "As-Fabricated and Heat-Treated Microstructures of the Ti-6Al-4V Alloy Processed by Selective Laser Melting."

[59] C. Qiu, G. A. Ravi, C. Dance, A. Ranson, S. Dilworth, and M. M. Attallah, "Fabrication of large Ti-6Al-4V structures by direct laser deposition," *Journal of Alloys and Compounds*, vol. 629, pp. 351–361, 2015.

[60] H. Atkinson and S. Davies, "Fundamental aspects of hot isostatic pressing: an overview," *Metallurgical and Materials Transactions A*, vol. 31A, no. December, pp. 2981–3000, 2000.

[61] P. Rangaswamy *et al.*, "Residual stresses in LENS?? components using neutron diffraction and contour method," *Materials Science and Engineering A*, vol. 399, no. 1–2, pp. 72–83, 2005.

[62] P. Mercelis and J. Kruth, “Residual stresses in selective laser sintering and selective laser melting,” *Rapid Prototyping Journal*, vol. 12, no. 5, pp. 254–265, 2006.

[63] D. J. Green, R. Tandon, and V. M. Sglavo, “Crack Arrest and Multiple Cracking in Glass Through the Use of Designed Residual Stress Profiles,” vol. 283, no. February, pp. 1295–1298, 1999.

[64] S. Wang, Y. Li, M. Yao, and R. Wang, “Compressive residual stress introduced by shot peening,” *Journal of Materials Processing Technology*, vol. 73, no. 1, pp. 64–73, 1998.

[65] A. S. Wu, D. W. Brown, M. Kumar, G. Gallegos, and W. E. King, “An Experimental Investigation into Additive Manufacturing Induced Residual Stresses in 316L Stainless Steel,” 2014.

[66] M. L. Griffith *et al.*, “Understanding thermal behavior in the LENS process,” pp. 107–113, 1999.

[67] E. R. Denlinger, J. C. Heigel, P. Michaleris, and T. A. Palmer, “Journal of Materials Processing Technology Effect of inter-layer dwell time on distortion and residual stress in additive manufacturing of titanium and nickel alloys,” *Journal of Materials Processing Tech.*, vol. 215, pp. 123–131, 2015.

[68] N. W. Klingbeil, J. L. Beuth, R. K. Chin, and C. H. Amon, “Residual stress-induced warping in direct metal solid freeform fabrication,” *International Journal of Mechanical Sciences*, vol. 44, no. 1, pp. 57–77, 2002.

[69] R. Jendrzejewski and G. Śliwiński, “Investigation of temperature and stress fields in laser cladded coatings,” *Applied Surface Science*, vol. 254, no. 4, pp. 921–925, 2007.

[70] A. Vasinonta and J. Beuth, “Process Maps for Controlling Residual Stress and Melt Pool Size in Laser-Based SFF Processes,” *Proceedings 2000 Solid Freeform Fabrication Symposium Solid Freeform Fabrication Symposium*, pp. 200–208, 2000.

[71] M. A. Russell, A. Souto-Iglesias, and T. I. Zohdi, “Numerical simulation of Laser Fusion Additive Manufacturing processes using the SPH method,” *Computer Methods in Applied Mechanics and Engineering*, vol. 341, pp. 163–187, Nov. 2018.

[72] M. Markl and C. Körner, “Multiscale Modeling of Powder Bed–Based Additive Manufacturing,” *Annu. Rev. Mater. Res.*, vol. 46, no. 1, pp. 93–123, Jul. 2016.

[73] T. Keller *et al.*, “Application of finite element, phase-field, and CALPHAD-based methods to additive manufacturing of Ni-based superalloys,” *Acta Materialia*, 2017.

[74] S. Sahoo and K. Chou, “Phase-field simulation of microstructure evolution of Ti–6Al–4V in electron beam additive manufacturing process,” *Additive Manufacturing*, vol. 9, pp. 14–24, Jan. 2016.

[75] L.-X. Lu, N. Sridhar, and Y.-W. Zhang, “Phase field simulation of powder bed-based additive manufacturing,” *Acta Materialia*, vol. 144, pp. 801–809, Feb. 2018.

[76] L.-Q. Chen, “Phase-Field Models for Microstructure Evolution,” *Annu. Rev. Mater. Res.*, vol. 32, no. 1, pp. 113–140, Aug. 2002.

[77] A. Rai, M. Markl, and C. Körner, “A coupled Cellular Automaton–Lattice Boltzmann model for grain structure simulation during additive manufacturing,” *Computational Materials Science*, vol. 124, pp. 37–48, Nov. 2016.

[78] O. Zinovieva, A. Zinoviev, and V. Ploshikhin, “Three-dimensional modeling of the microstructure evolution during metal additive manufacturing,” *Computational Materials Science*, 2018.

[79] A. Zinoviev, O. Zinovieva, V. Ploshikhin, V. Romanova, and R. Balokhonov, “Evolution of grain structure during laser additive manufacturing. Simulation by a cellular automata method,” *Materials & Design*, vol. 106, pp. 321–329, Sep. 2016.

[80] J. A. Koepf, M. R. Gotterbarm, M. Markl, and C. Körner, “3D multi-layer grain structure simulation of powder bed fusion additive manufacturing,” *Acta Materialia*, vol. 152, pp. 119–126, Jun. 2018.

[81] Y. Lian, S. Lin, W. Yan, W. K. Liu, and G. J. Wagner, “A parallelized three-dimensional cellular automaton model for grain growth during additive manufacturing,” *Comput Mech*, vol. 61, no. 5, pp. 543–558, May 2018.

[82] M. Rappaz and C. A. Gandin, “Probabilistic modelling of microstructure formation in solidification processes,” *Acta Metallurgica Et Materialia*, vol. 41, no. 2, pp. 345–360, 1993.

[83] C. A. Gandin, J. L. Desbiolles, M. Rappaz, and P. Thévoz, “A three-dimensional cellular automaton-finite element model for the prediction of solidification grain structures,” *Metallurgical and Materials Transactions A: Physical Metallurgy and Materials Science*, 1999.

[84] T. M. Rodgers, J. D. Madison, and V. Tikare, “Simulation of metal additive manufacturing microstructures using kinetic Monte Carlo,” *Computational Materials Science*, vol. 135, pp. 78–89, Jul. 2017.

[85] S. Haeri, Y. Wang, O. Ghita, and J. Sun, “Discrete element simulation and experimental study of powder spreading process in additive manufacturing,” *Powder Technology*, vol. 306, pp. 45–54, Jan. 2017.

[86] J. C. Steuben, A. P. Iliopoulos, and J. G. Michopoulos, “Discrete element modeling of particle-based additive manufacturing processes,” *Computer Methods in Applied Mechanics and Engineering*, vol. 305, pp. 537–561, Jun. 2016.

[87] S. A. Khairallah and A. Anderson, “Mesoscopic simulation model of selective laser melting of stainless steel powder,” *Journal of Materials Processing Technology*, vol. 214, no. 11, pp. 2627–2636, Nov. 2014.

[88] J. Goldak, A. Chakravarti, and M. Bibby, “A new finite element model for welding heat sources,” *Metallurgical Transactions B*, vol. 15, no. 2, pp. 299–305, Jun. 1984.

[89] L. Wang, S. Felicelli, Y. Gooroochurn, P. T. Wang, and M. F. Horstemeyer, “Optimization of the LENS® process for steady molten pool size,” *Materials Science and Engineering: A*, vol. 474, no. 1–2, pp. 148–156, Feb. 2008.

[90] X. Lu *et al.*, “Residual stress and distortion of rectangular and S-shaped Ti-6Al-4V parts by Directed Energy Deposition: Modelling and experimental calibration,” *Additive Manufacturing*, vol. 26, pp. 166–179, Mar. 2019.

[91] P. Michaleris, “Modeling metal deposition in heat transfer analyses of additive manufacturing processes,” *Finite Elements in Analysis and Design*, vol. 86, pp. 51–60, 2014.

[92] C. H. Fu and Y. B. Guo, “3-Dimensional Finite Element Modeling of Selective Laser Melting Ti-6Al-4V Alloy,” pp. 1129–1144.

[93] C. Geuzaine and J.-F. Remacle, “Gmsh: A 3-D finite element mesh generator with built-in pre- and post-processing facilities,” *Int. J. Numer. Meth. Engng*, vol. 79, no. 11, pp. 1309–1331, Sep. 2009.

[94] M. F. Sanner, “Python: A Programming Language for Software Integration and Development,” p. 7.

[95] A. Ranellucci, “Slic3r Reference Manual 1.2.9.” 2018.

[96] M. J. Dantin, W. M. Furr, and M. W. Priddy, “Effects of dual-wave pyrometer-datasets on a predictive finite element thermal model of a Ti-6Al-4V thin wall constructed via LENS.”

[97] K. C. Mills, *Recommended Values of Thermophysical Properties for Selected Commercial Alloys*. Cambridge: Woodhead Publishing Ltd., 2002.

[98] G. J. Marshall, S. M. Thompson, and N. Shamsaei, “Data indicating temperature response of Ti-6Al-4V thin-walled structure during its additive manufacture via Laser Engineered Net Shaping,” *Data in Brief*, vol. 7, pp. 697–703, 2016.

[99] D. A. Kriczky, J. Irwin, E. W. Reutzel, P. Michaleris, A. R. Nassar, and J. Craig, “3D spatial reconstruction of thermal characteristics in directed energy deposition through optical thermal imaging,” *Journal of Materials Processing Technology*, vol. 221, pp. 172–186, 2015.